Grant Agreement No: 101096307

Full Title: THz Industrial Mesh Networks in Smart Sensing and Propagation Environments

Start date: 01/01/2023

End date: 31/12/2025

Duration: 36 Months

Deliverable D5.3

Design fabrication and verification of high directivity and beam steering antennas at THz frequencies

Document Type	Deliverable
Title	D5.3 - Design fabrication and verification of high directivity and beam steering antennas at THz frequencies
Contractual due date	30/03/2025 (M28)
Actual submission date	11/04/2025
Nature	Report
Dissemination Level	PUB
Lead Beneficiary	ANTERAL
Responsible Author	Victor Torres (ANTERAL)
Contributions from	Guillaume Ducournau (CNRS), Frédéric Dutin (CNRS)
Reviewers	Tommaso Zugno (HWDU), Simon Haubmann (USTUTT)

Revision history

Version	Issue Date	Changes	Contributor(s)
v0.1	20/02/2025	Initial version	V. Torres (ANTERAL)
v0.2	05/04/2025	Add experimental results for LWA and PDLA	G. Ducournau and F. Dutin (CNRS)
v0.3	09/04/2025	Review	T. Zugno (HUAWEI)
v0.4	11/04/2025	Review	S. Haubmann (U. STUTTGART)
v1.0	11/04/2025	Final version	V. Torres (ANTERAL)

Table of Contents

List of Abbreviations

KPI	Key Performance Indicator
LWA	Leaky Wave Antenna
PDLA	Phase Delay Line Antenna
PoC	Proof of Concept
THz	Terahertz

Executive Summary

This document offers an overview of the different types of antennas designed, fabricated and validated for the TIMES PoCs: it includes the simulated and measured KPIs of these antennas, as inputs for PoC scenarios definition/refinements (distances, location of devices, …).

This document offers a comprehensive overview of the various antenna types that have been designed, fabricated, and validated specifically for the TIMES (THz Industrial Mesh Networks in Smart Sensing and Propagation Environments) Proofs of Concept (PoCs). This includes a detailed presentation of both the simulated and measured Key Performance Indicators (KPIs) for these antennas. This information is intended to serve as crucial inputs for the definition and refinement of the PoC scenarios, particularly concerning aspects like distances between devices and their optimal locations.

The document dedicates significant attention to two primary categories of antennas: high directivity antennas (discussed in Section 2) and beam steering antennas (detailed in Section 3). For the high directivity antennas, the document explores their motivation due to the challenges of THz communication in industrial environments, such as high path loss and the need for long-distance testing ranges. The design strategy, simulation results showing far-field and near-field performance, fabricated prototypes, and thorough validation results are presented, including measured return loss, directivity, beamwidth, and sidelobe levels. These KPIs and their compliance with the project's requirements directly inform the achievable link distances and the suitability of these antennas for point-to-point communication in PoC 1 scenarios.

Similarly, for the beam steering antennas, which include the Leaky Wave Antenna (LWA) and the Phase Delay Line Antenna (PDLA), the document details their motivation for providing flexibility in directing radio waves in complex industrial environments, mitigating interference, and enabling efficient spatial multiplexing. The design and simulation phases for both LWA and PDLA are covered, followed by the mechanical design, fabricated prototypes, and validation results. The measured KPIs for these beam steering antennas, such as steering angle, gain, and return loss, are critical inputs for defining the dynamic communication scenarios of PoC 2, influencing the placement and adaptability of devices within the THz industrial mesh network. The document's findings, including the achieved steering capabilities and gain figures, directly impact the feasibility and performance expectations of the defined PoC scenarios

1. Introduction

This document, Deliverable D5.3, presents a detailed description of the design, fabrication, and verification of high directivity and beam steering antennas operating in the Terahertz (THz) frequency range. This work is part of the TIMES (THz Industrial Mesh Networks in Smart Sensing and Propagation Environments) project, which aims to develop THz mesh networks for industrial applications. The need for these antennas arises from the inherent challenges of THz communication in industrial environments, including high signal attenuation and the complexity of environments with obstacles and reflections.

In this context, two main types of antennas are explored and developed: high directivity antennas, essential for path loss compensation in long-range communications, and beam steering antennas, crucial for their flexibility in directing radio waves and mitigating interference in dynamic environments. The document details the motivation behind the development of each antenna type, the design strategies implemented, the simulation results, the fabrication processes of prototypes, and the experimental validation results in relation to the Key Performance Indicators (KPIs) defined for the project. Finally, the conclusions obtained from this work are presented, highlighting the performance achieved and its relevance to the future proof-of-concept (PoCs) of the TIMES project

1.1 Scope

This deliverable provides a summary of the antenna designs, simulations and experimental measurements.

1.2 Audience

This deliverable is intended for internal use by the TIMES Consortium and for public dissemination.

1.3 Structure

The rest of the document is structured as follows:

- Section 2 presents the high directivity antennas.
- Section 3 presents the beam-steering antennas: leaky wave approach and phase delay line.

Finally, a brief summary is given in the conclusion section.

2 Development of high directivity antennas

This section describes the development of high-directivity antennas that will be used as components of the demonstration hardware in the PoC. It presents the motivation behind this development, the design strategy, the manufactured prototypes, and the simulation and measurement results.

2.1 Motivation

High-gain antennas are essential for THz communication in industrial environments due to several key factors related to the characteristics of THz waves and the specific challenges of such environments:

- **Path loss compensation**: THz waves experience high attenuation during propagation, especially over long distances. High-gain antennas are necessary to compensate for these losses and ensure that the signal reaches the receiver with sufficient power to be detected and processed correctly.
- **Long-distance testing range**: To achieve the required distances in long-range proof-of-concept (PoC) tests, high-gain antennas are needed. These antennas help overcome free-space signal losses, which are significant at THz frequencies. Also, the PoC includes P2P communication over a reconfigurable reflective surface, which intrduces addtional attenuation to the high path losses
- **High directivity and narrow beams**: High gain implies high directivity, resulting in a narrow beam. In a complex industrial environment with many obstacles and potential reflections, it is crucial to precisely direct the beam to reduce interference and improve signal quality. Highly directive antennas concentrate signal energy in a specific direction, increasing transmission efficiency.
- **Complex environments**: Industrial environments are complex due to the presence of machinery, metal structures, and other obstacles that can cause reflections and multipath propagation. High-directivity antennas help mitigate the issues caused by these conditions.
- **Data communication requirements**: For data communication between fixed points in industrial environments, high-gain antennas are required to achieve the necessary distances in long-range PoC tests.

Numerous high-gain antenna architectures exist, each optimized for specific applications [1]. Parabolic antennas, commonly utilized in satellite communications, employ a parabolic reflector to focus electromagnetic waves into a highly collimated beam. Yagi-Uda antennas, frequently deployed in television reception and amateur radio, comprise an array of parallel elements configured to enhance directional gain. Horn antennas, recognized for their broad bandwidth, are extensively used in microwave applications and radio astronomy. Patch antennas, or microstrip antennas, offer compact form factors and seamless integration into electronic devices, making them ideal for mobile and satellite communications. Helical antennas, characterized by circular polarization, are advantageous in scenarios requiring both high gain and wide bandwidth, such as satellite and deep-space communication. Each of these antenna types contributes to optimizing electromagnetic wave propagation across diverse technical domains.

However, not all these antenna configurations are suitable for operation within the THz spectrum, particularly in the 220–330 GHz range. Constraints in fabrication precision and the pronounced losses at high frequencies significantly narrow the feasible selection. The inherent topology of certain antennas and the stringent tolerances required for their manufacture may render some designs impractical. Furthermore, the nature of RF signal generation dictates the choice of antenna feeding mechanisms, which subsequently constrain the viable antenna architectures.

At frequencies approaching 300 GHz, achieving substantial gain necessitates the use of reflector or lens-based systems, typically fed by horn antennas, which themselves rely on waveguide structures for excitation. For this specific implementation, lens-coupled horn antennas have been selected. The integration of a dielectric lens enables a reduction in the physical dimensions of the horn while preserving the desired beam characteristics. Without a lens, attaining the requisite directivity would demand excessively elongated horn structures, potentially exceeding practical manufacturing limitations.

Lens-coupled horn antennas were preferred over reflector-based systems due to their simplified fabrication, enhanced structural integrity, and compact footprint. The feed-lens assembly ensures high directivity while simultaneously improving mechanical robustness and alignment precision. By suppressing spurious radiation, this configuration optimizes system performance, rendering it particularly suitable for the stringent requirements of PoC evaluations in the THz regime. The selection of horn antennas with integrated lenses reflects a deliberate balance between manufacturability and the necessity for precise, high-gain performance in complex deployment environments.

Additionally, planar antenna solutions were deemed unsuitable due to the inherent propagation losses within the substrate. These losses become particularly pronounced due to the extensive and intricate feed networks required to achieve high gain, necessitating a large number of radiating elements. Moreover, designing an efficient transition between the waveguide-based output of the active component and the planar antenna—one that ensures broadband operation with minimal insertion loss and optimal impedance matching—poses significant engineering challenges.

In [2], different inter-device scenarios are presented, along with a series of requirements that can be addressed using high-gain antennas with lenses. Additionally, a set of KPIs was introduced in [3].

Table 1. High Gain Antennas KPIs.

Parameter	Condition and value	Remarks
Return loss	< -10 dB	Across the full frequency bandwidth
Directivity	> 45 dBi	Maximum value
Mean beamwidth	< 2 degrees	At - 3dB
Losses	< 1.5 dB	-
Sidelobe level	< -30 dB	-

According to these requirements, the chosen design features a short horn antenna in the form of a compact feed that effectively illuminates a dielectric lens. This feed-lens system is enclosed in a metallic cylinder to minimize radiation at undesired angles and reduce the intensity of secondary lobes. However, using a lens introduces additional propagation losses, necessitating the selection of low-loss materials suitable for this frequency range, such as Teflon or high-performance polymers.

2.2 Design strategy

A hyperbolic lens profile is employed due to its ability to minimize the effective volume of the lens, thereby reducing propagation losses while enabling efficient fabrication through conventional milling techniques [4].

Figure 1 presents the governing equations defining the hyperbolic contour used for the lens profile design, accompanied by a conceptual illustration. The focal length of the lens is denoted as FL, while ε_r represents the relative permittivity of the lens material, and n corresponds to its refractive index. Given these parameters, the hyperbola's design coefficients a and b are derived. The phase center of the feed is positioned at $x = a - FL$, ensuring that all emitted rays originating from this point and interacting with the lens are collimated towards infinity. Consequently, the emerging wavefront at the lens exit approximates a planar wave, leading to enhanced directivity and a reduced beamwidth relative to the standalone feed source. It would possible to reduce the overall size by an additional diverging lens, but the overall design requirements are fulfilled with a single lens.

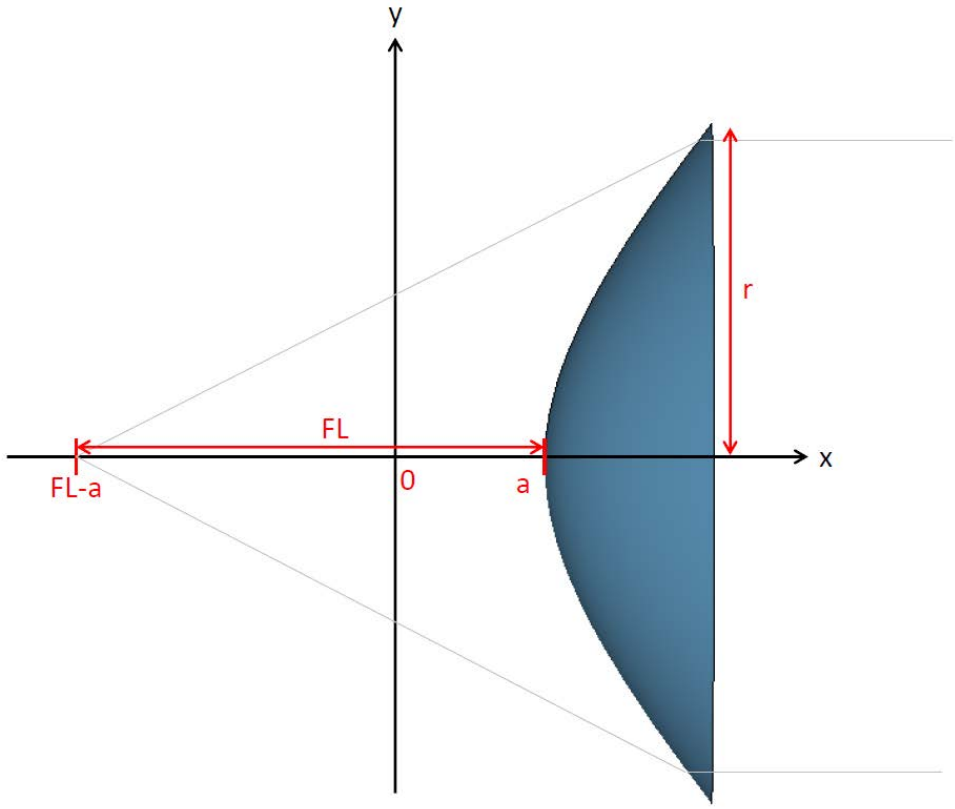

$$\frac{x^2}{a^2} - \frac{y^2}{b^2} = 1$$

$$a = \frac{FL}{n+1}$$

$$b = FL\sqrt{\frac{n-1}{n+1}}$$

$$n = \sqrt{\varepsilon_r}$$

Figure 1. Sketch of hyperbolic lens and associated formulas.

Several polymers are evaluated through simulation, with PE-1000 ultimately selected as the optimal material due to its balanced combination of low weight, minimal dielectric losses, manufacturability, and favorable mechanical and thermal properties. Table 2 presents the key electrical and mechanical properties of PE-1000 (Ultra-High Molecular Weight Polyethylene). These characteristics render PE-1000 particularly suitable for applications requiring a synergistic integration of robust mechanical performance and advantageous electromagnetic properties, such as in high-frequency antenna and dielectric lens systems

Table 2. Main properties of PE-1000.

Property	Value	Unit
Density	0.93 - 0.94	g/cm³
Tensile strength	20 - 40	MPa
Elastic modulus	600 - 800	MPa
Elongation at break	300 - 350	%
Shore D hardness	63 - 66	-
Coefficient of friction	0.10 - 0.22	-
Operating temperature	-150 to +80	°C
Thermal conductivity	0.41	W/m·K
Dielectric constant	2.1 - 2.3	-
Volume resistivity	>10^14	Ω·cm
Dielectric strength	50	kV/mm
Dielectric loss factor	0.0004 - 0.0009	-

The design process has proceeded as follows. Initially, the feed and lens geometries are modeled and optimized using GRASP [5]. The feed structure consists of a short pyramidal horn, with a standard WR-3.4 waveguide port employed as the input interface to accommodate the operational bandwidth. The optimization of the feed length and aperture dimensions is conducted in relation to the lens positioning and overall lens size. The primary design criterion is achieving a beamwidth of less than two degrees. To meet this requirement, a compact feed-lens system is developed, ensuring minimal spatial footprint while maintaining the desired radiation characteristics.

Following the initial design in GRASP, the complete assembly, including the metallic enclosure, is simulated in CST [6] to validate performance consistency and confirm that the presence of the metallic cylinder does not degrade the beamwidth beyond the specified limits. The metallic enclosure is further optimized to minimize overall weight and size while preserving the necessary structural and electromagnetic performance characteristics of the lens system.

2.3 Simulation results

Two different types of simulations are performed to calculate the radiation pattern in the far field and near field. This is because, depending on the nature of the PoC, the devices establishing communication may be in either situation.

The far field, also known as the far radiation zone, is the region where the structure of the electromagnetic field simplifies, and the components of the electric and magnetic fields are perpendicular to each other and to the direction of wave propagation. In this region, the antenna's radiation pattern stabilizes and the electromagnetic waves behave as plane waves.

The minimum distance R at which the far field begins for an antenna can be calculated using the following formula:

$$R \geq \frac{2D^2}{\lambda}$$

Where D is the maximum dimension of the antenna and λ is the wavelength of the signal. Therefore, for the 220 – 330 GHz band, we obtain a far field region starting, approximately, at 75 m (220 GHz) and 112 m (330 GHz). Therefore, for the inter-device scenario of the PoC, where the link distance are approximately 30 meters, near field results are of high interest.

Figure 2 shows the 0 deg, 45 deg and 90 deg copolar and 45 deg crosspolar farfield cuts at f = 220GHz, f = 275 GHz and f = 330 GHz. Figure 3, shows the same results but in nearfield, at a distance of 30 meters.

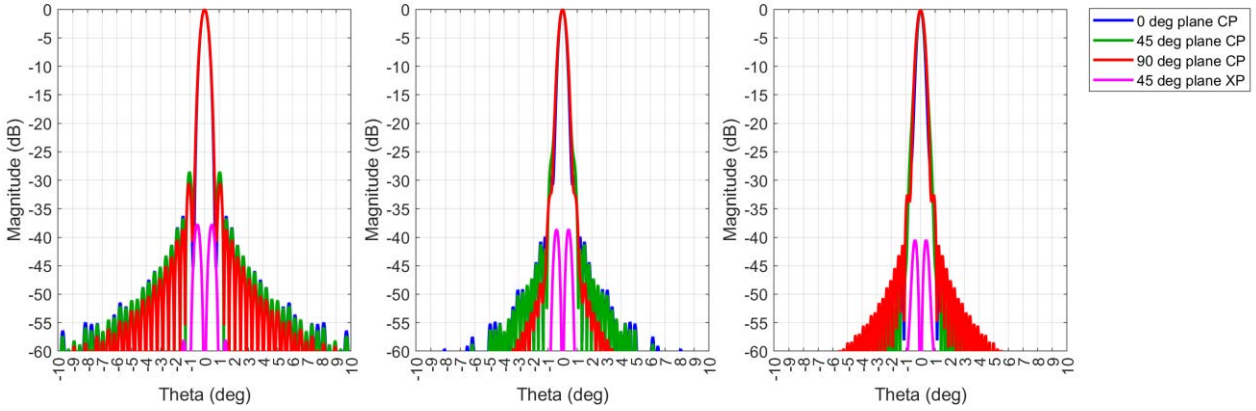

Figure 2. Far field cuts for planes of interest @220GHz, @275GHz and @330GHz.

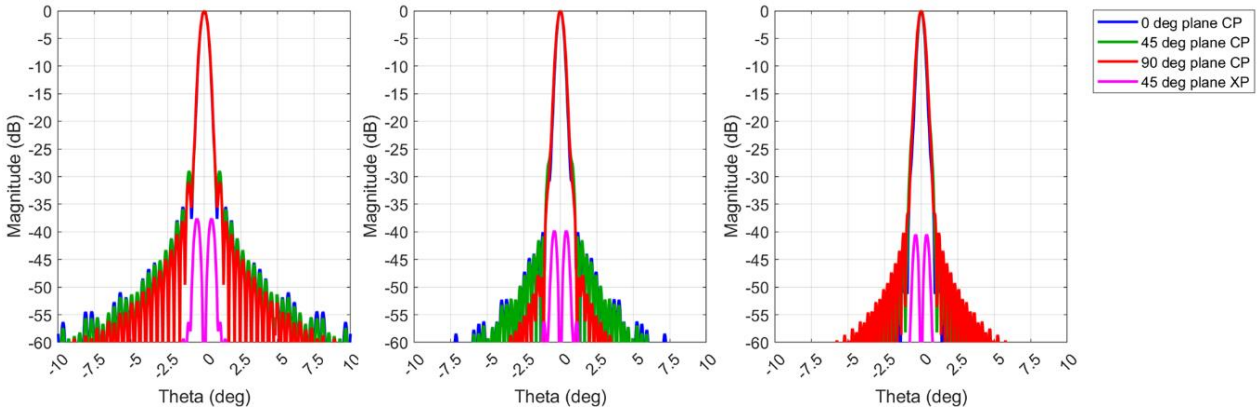

Figure 3. Near field cuts for planes of interest @220GHz, @275GHz and @330GHz.

It can be clearly seen that the far field and near field results are very similar. The specific beamwidth calculations for the E and H planes, for the two previous situations, are presented in Figures 4 and 5.

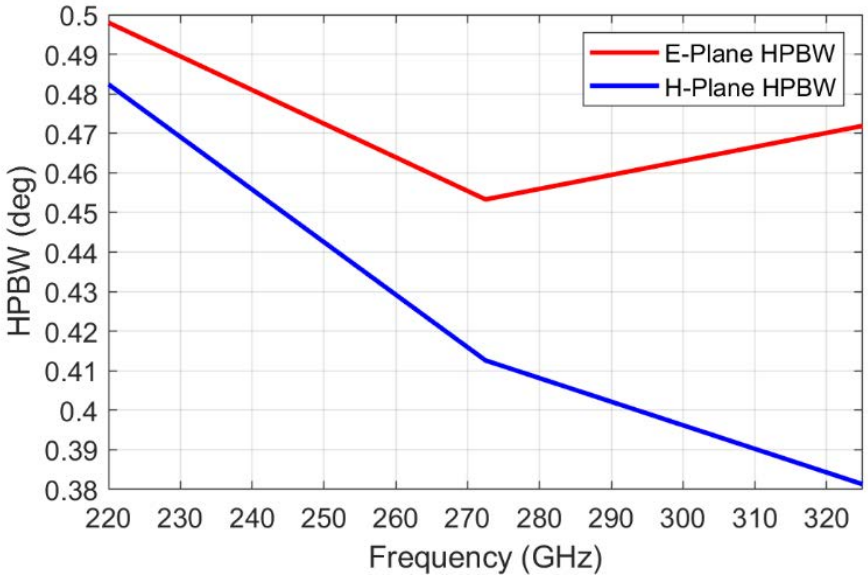

Figure 4. Half Power Beamwidth in far field.

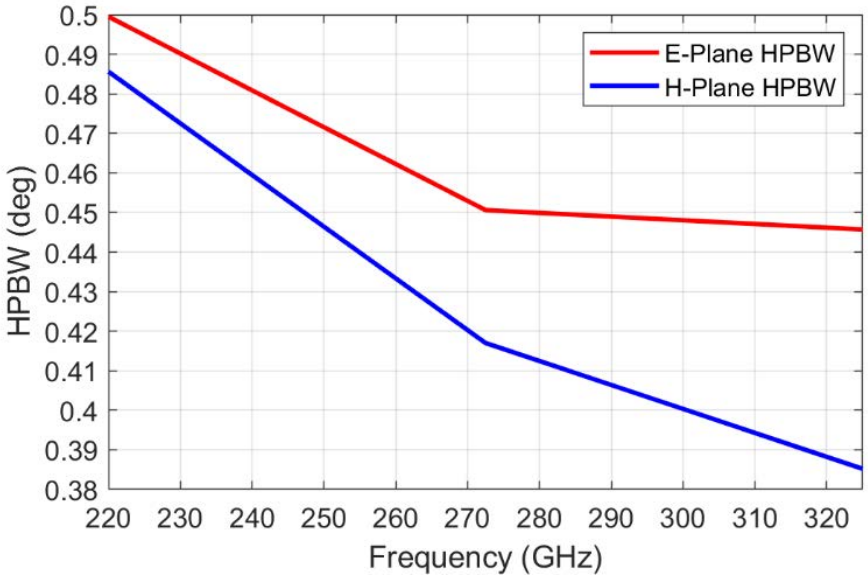

Figure 5. Half Power Beamwidth in near field at 30 m.

For both scenarios, the antenna emits a beamwidth smaller than 0.5 degrees. Both results are very similar. This implies, as corroborated by the simulation, that the directivity is higher than 50 dBi across the entire bandwidth. Additionally, the results show that the secondary lobes are below 30 dB.

2.4 Fabricated prototypes

Once the design is validated in simulation, an appropriate mechanical model is developed to provide sufficient robustness for assembling the different parts and to ensure a highly precise alignment between the feed and the lens. The metallic enclosure is designed to optimize the total weight and size of the system by reducing the thickness of the outer cylindrical metal part to less than 2 mm. The main characteristics of the complete system are shown in Table 3.

Table 3. Specifications of the high gain lens horn antenna.

Horn antenna with hyperbolic lens	
Material	Body: Aluminum
	Lens: PE-1000
Frequency Bandwidth	220 – 330 GHz
Input	WR-3.4 rectangular waveguide 300 × 420 µm
Length	193 mm
Diameter	226 mm
Metal Thickness	1.08 mm
Weight	2431 g

A 3D model of the final aspect of the antenna is shown in Figure 6. The left image shows a perspective of the lens face. The central image shows the rear part. It can be appreciated in grey, the feed with the standard input waveguide WR-3. The right image shows a cross-section view where the lens inside the antenna can be seen.

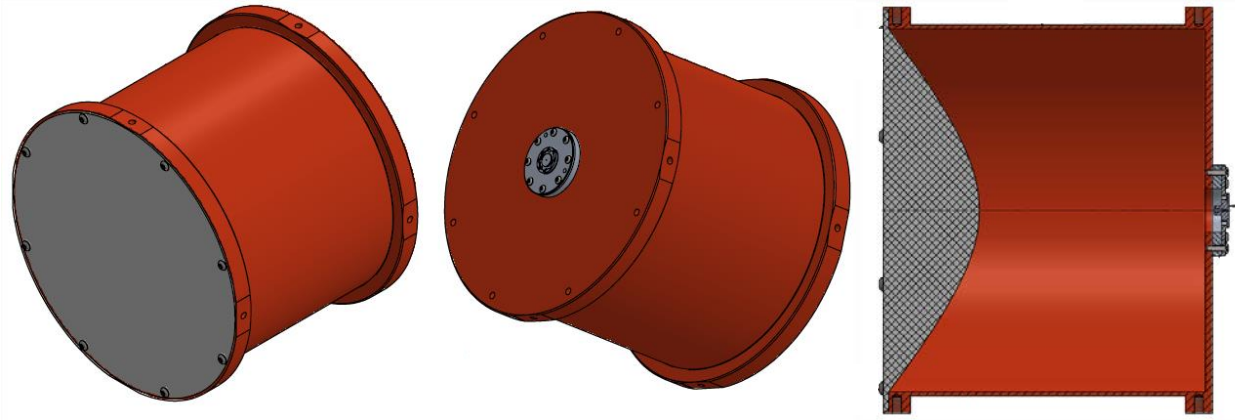

Figure 6. Front, rear and side schematic views of the high gain lens horn antenna.

Two prototypes have been manufactured according to the optimized design obtained from simulation. The prototypes have been fabricated in three parts: lens, feed, and cylinder. The main manufacturing technique

used was milling, although wire EDM (Electrical Discharge Machining) was also employed for the feed due to the small dimensions inside the waveguide.

Figure 7 shows a diagram with the overall dimensions and specifications of the manufactured prototype. Figure 8 presents actual photographs of one of the prototypes.

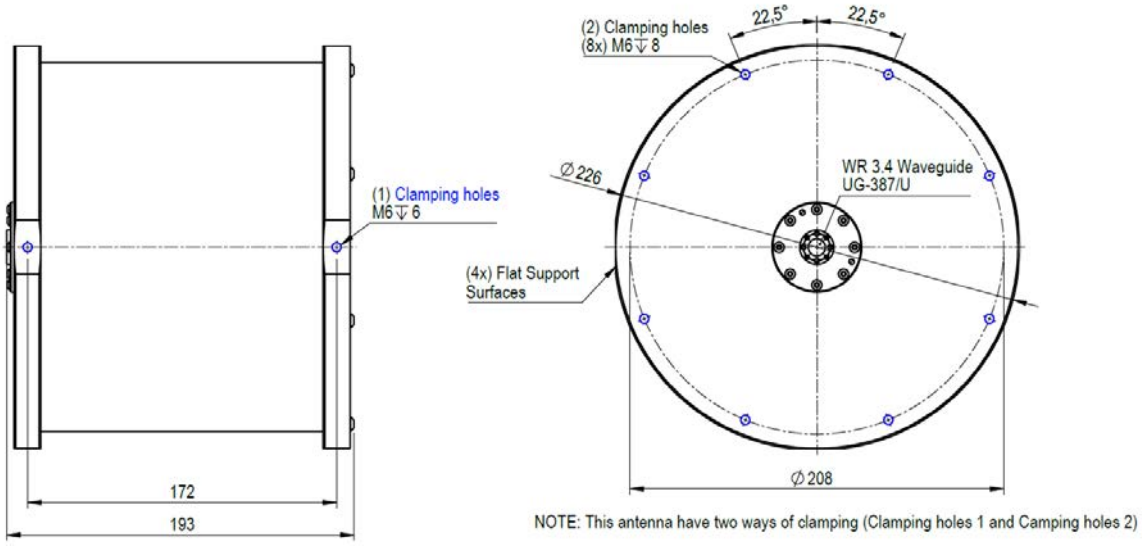

Figure 7. Drawing with side and rear view of the fabricated prototype.

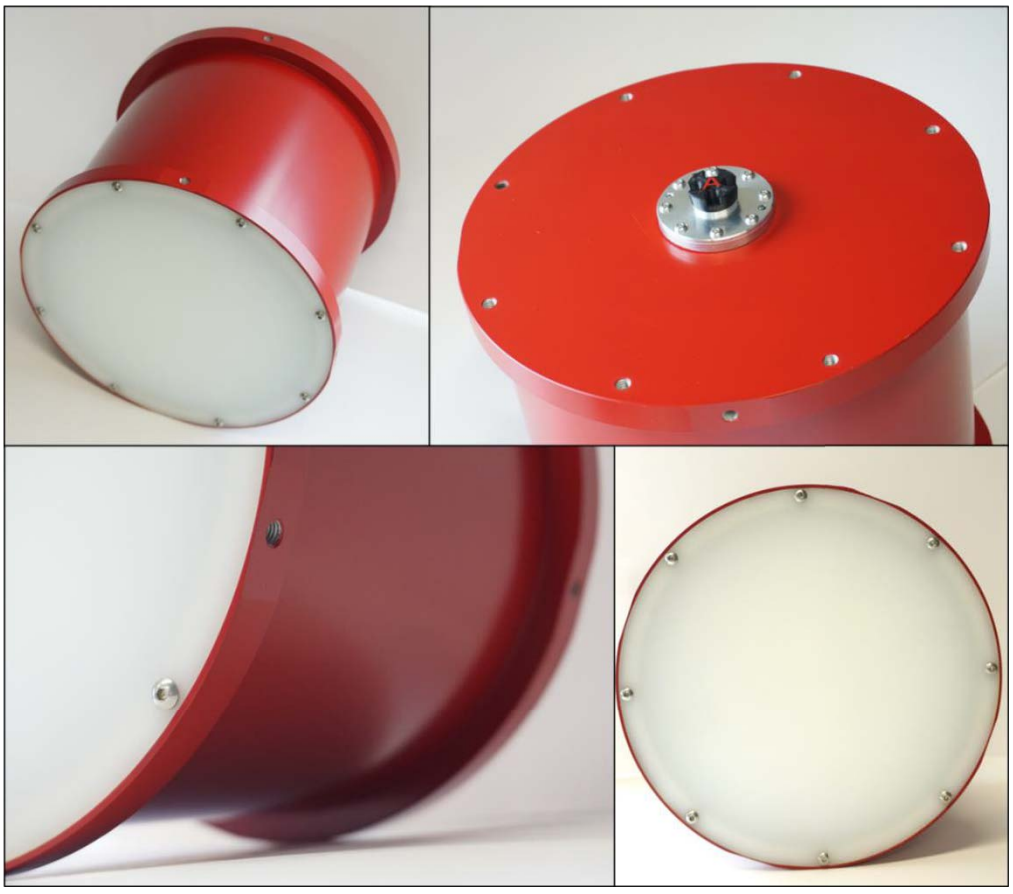

Figure 8. Pictures of the fabricated prototype.

2.5 Validation results

The validation of the prototypes is necessary to confirm their proper functioning according to the defined KPIs. The measurements are carried out in Anteral's characterization laboratory using a Keysight PNA-X N5242B vector network analyzer.

The prototype to be measured is connected to a frequency extender head from VDI, capable of transmission and reception in the 220 GHz to 330 GHz band. A near-field probe, also manufactured by Anteral, is used as the receiver, connected to another frequency extender head with reception-only capability.

The measurement process is divided into two steps:

1. A one-port calibrated measurement to assess return losses (S11) and verify the antenna's impedance matching in terms of delivered power.
2. A planar field measurement covering an area of 220 x 220 mm with a 2 mm step, corresponding to 0.45λ. This area is defined by a drop of more than 30 dB relative to the maximum. With this magnitude and phase measurement at each point of the planar field, the far-field radiation pattern can be calculated [7]. This mathematical calculation has been developed internally at Anteral.

The following images show several photographs of the measurement setup.

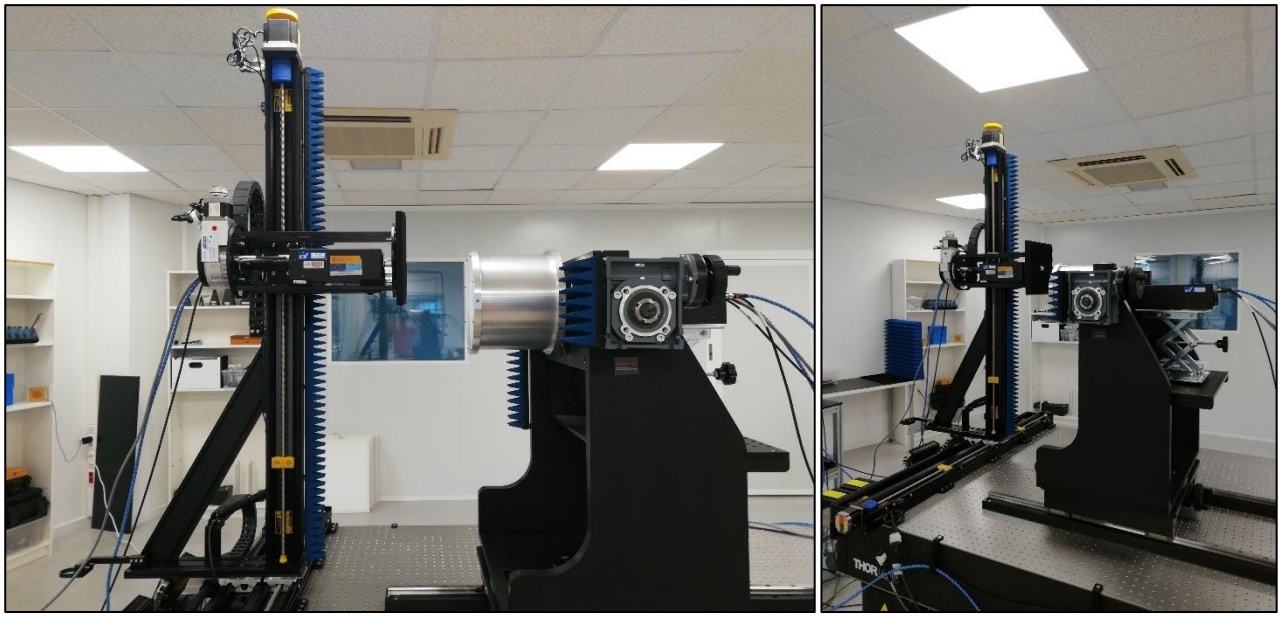

Figure 9. Measurement set-up.

Below, the results of the first manufactured prototype, identified as SN4641, are presented first, followed by those of the second prototype, identified as SN5248.

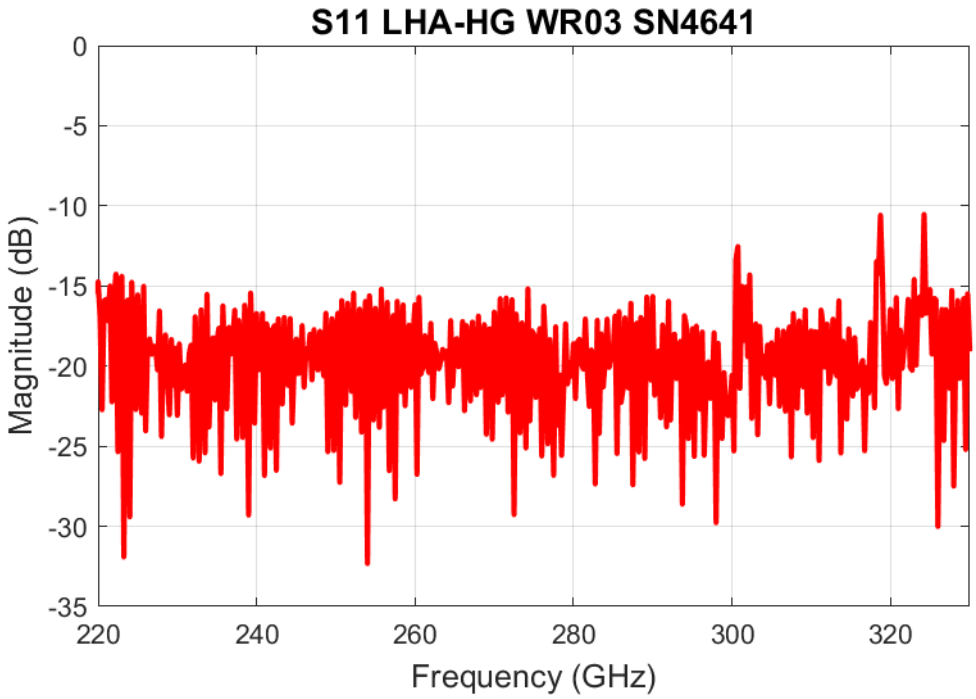

Figure 10. Measured S11 of prototype 1.

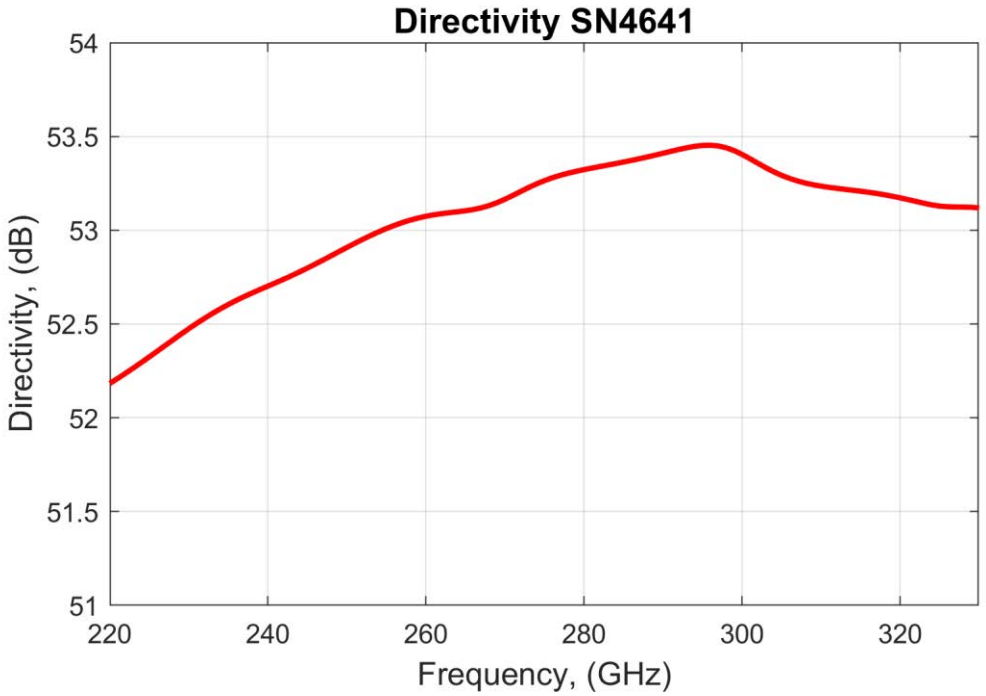

Figure 11. Measured directivity of prototype 1.

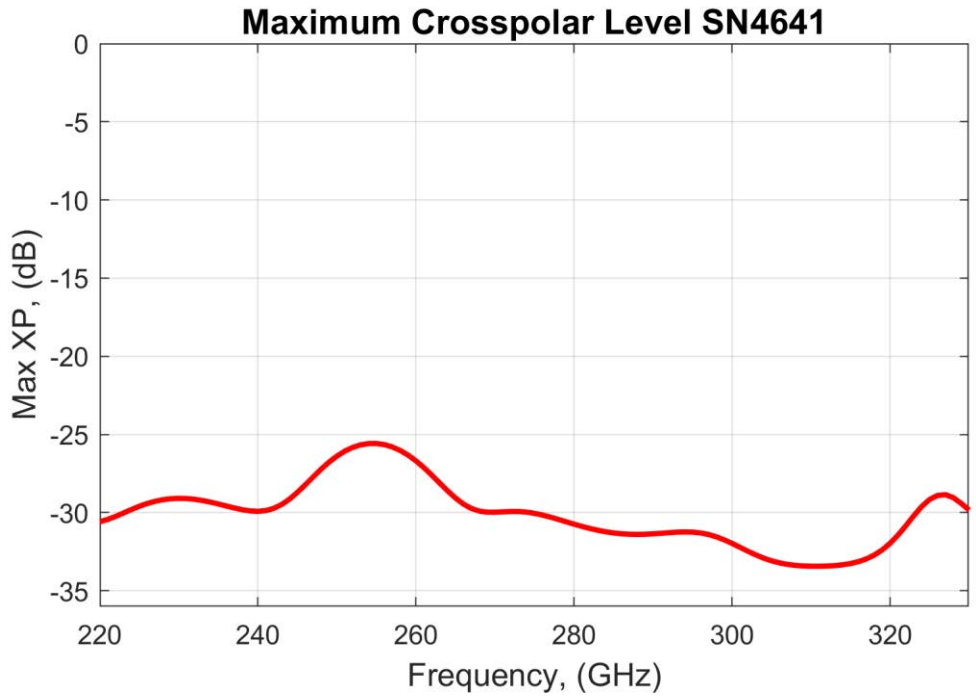

Figure 12. Max. measured crosspolar level of prototype 1.

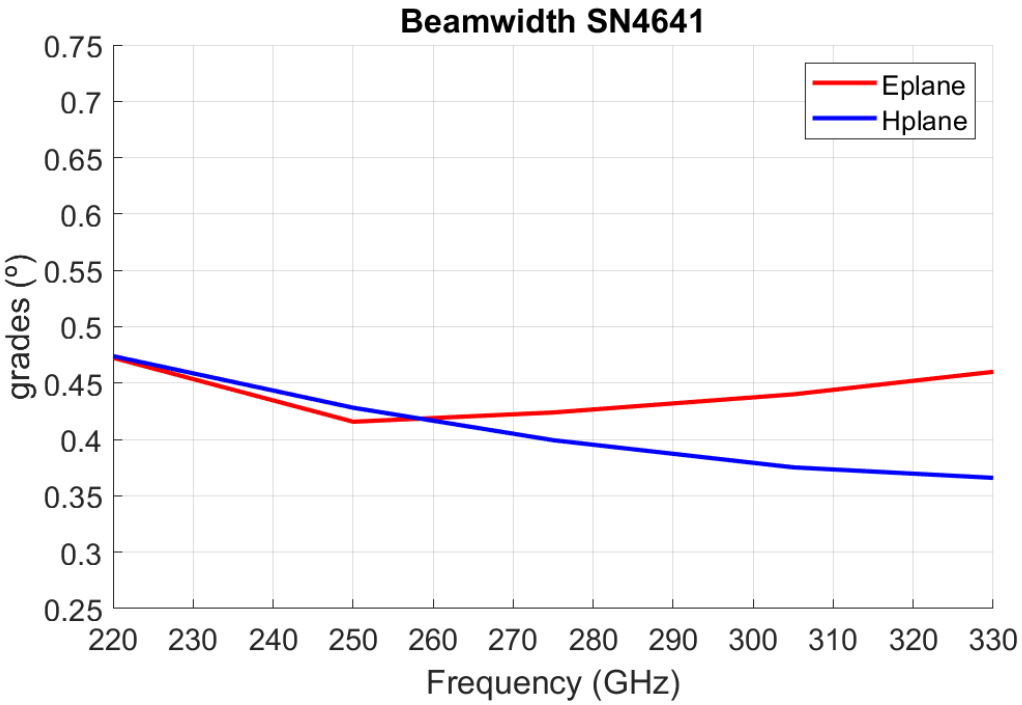

Figure 13. Beamwidth measured of prototype 1.

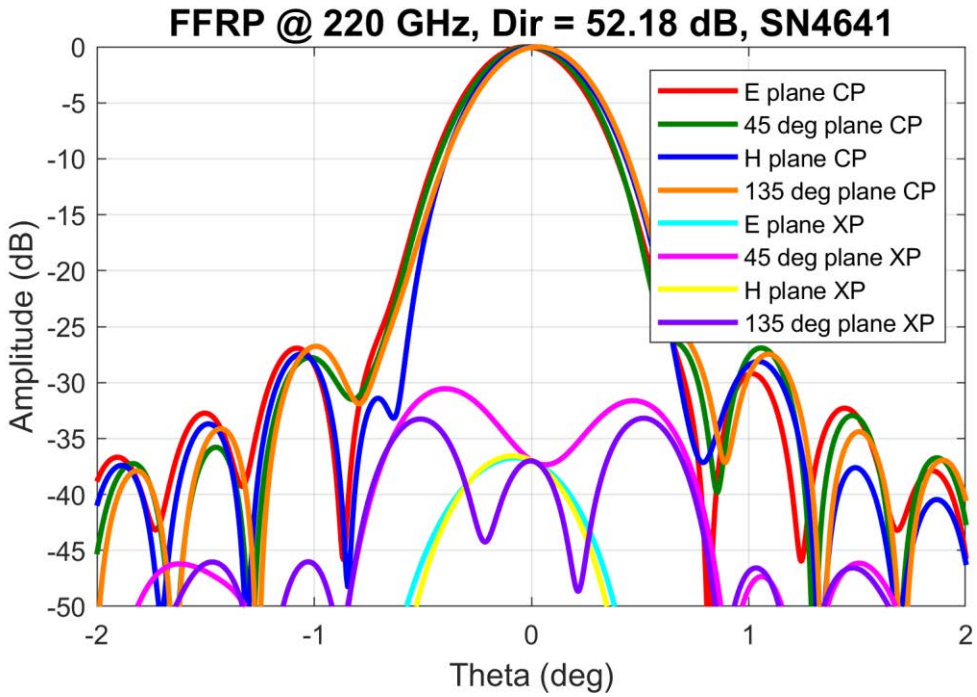

Figure 14. Measured far field radiation pattern at 220 GHz of prototype 1.

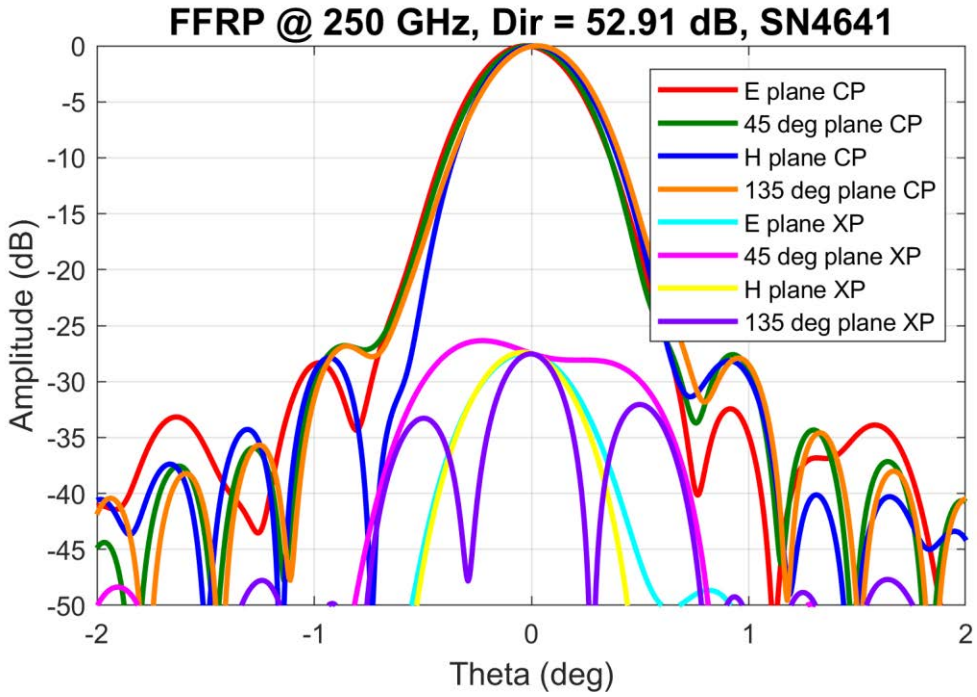

Figure 15. Measured far field radiation pattern at 250 GHz of prototype 1.

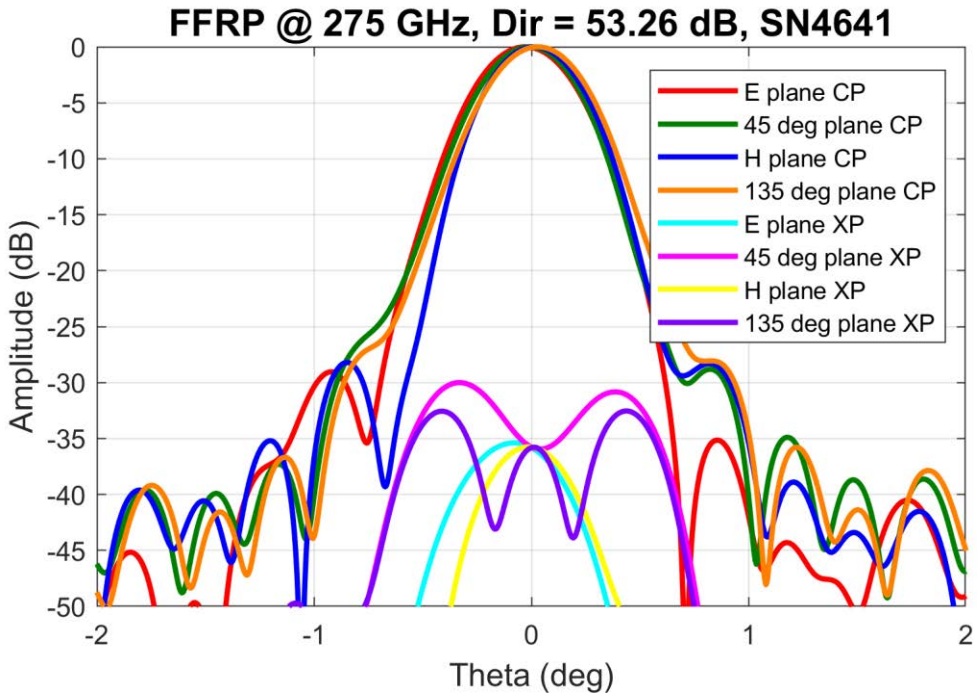

Figure 16. Measured far field radiation pattern at 275 GHz of prototype 1.

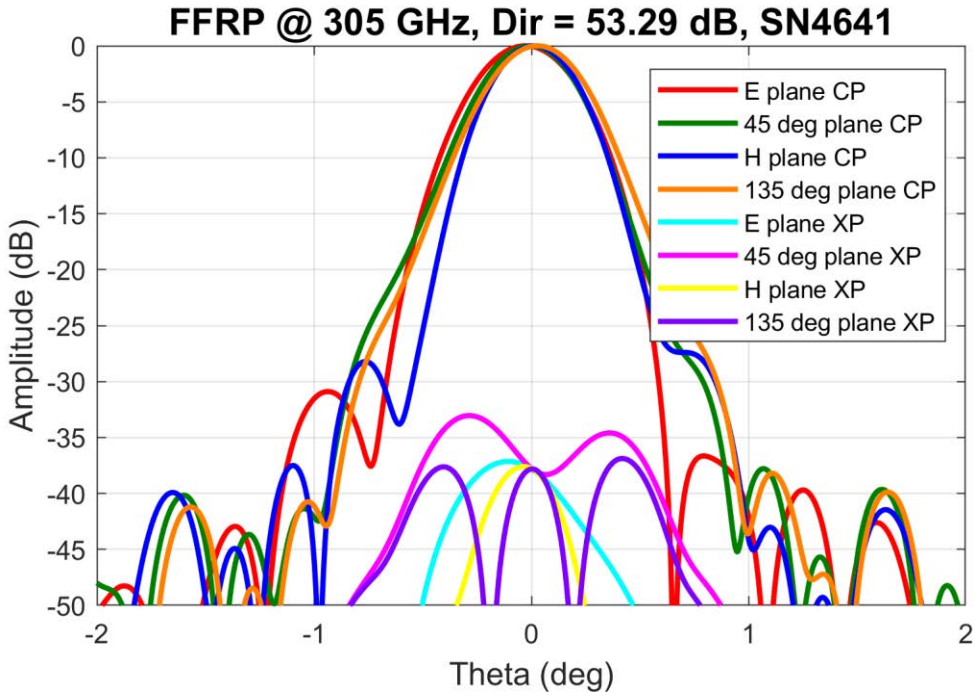

Figure 17. Measured far field radiation pattern at 305 GHz of prototype 1.

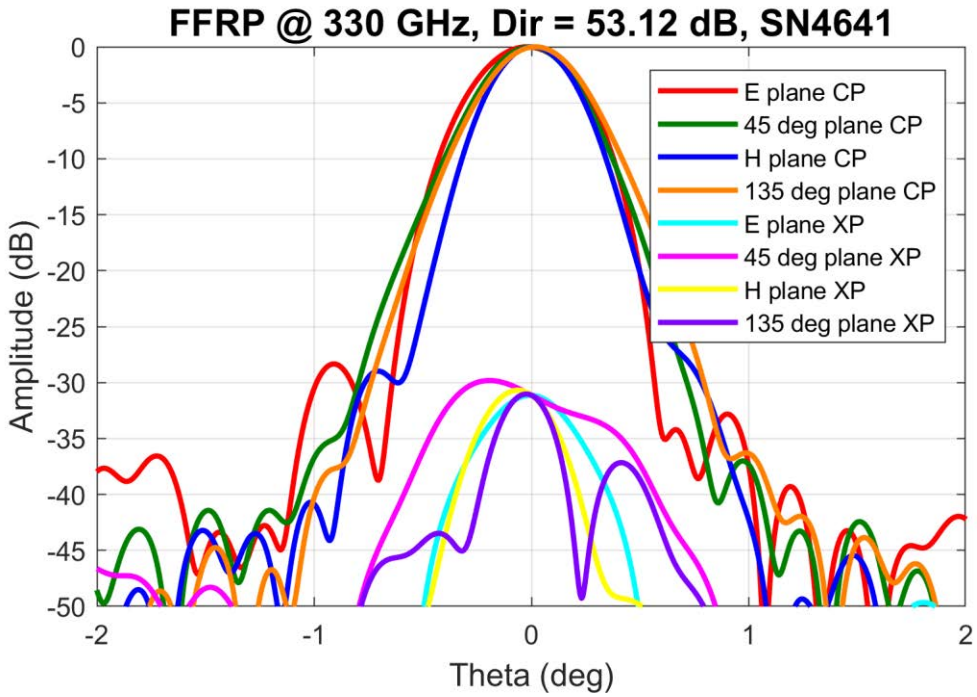

Figure 18. Measured far field radiation pattern at 330 GHz of prototype 1.

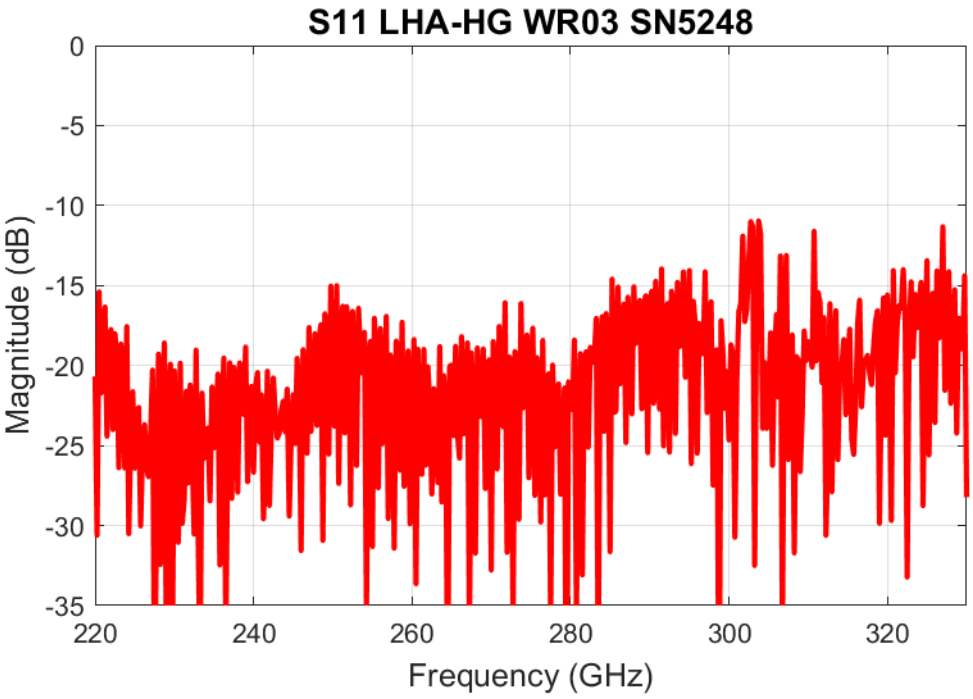

Figure 19. Measured S11 of prototype 2.

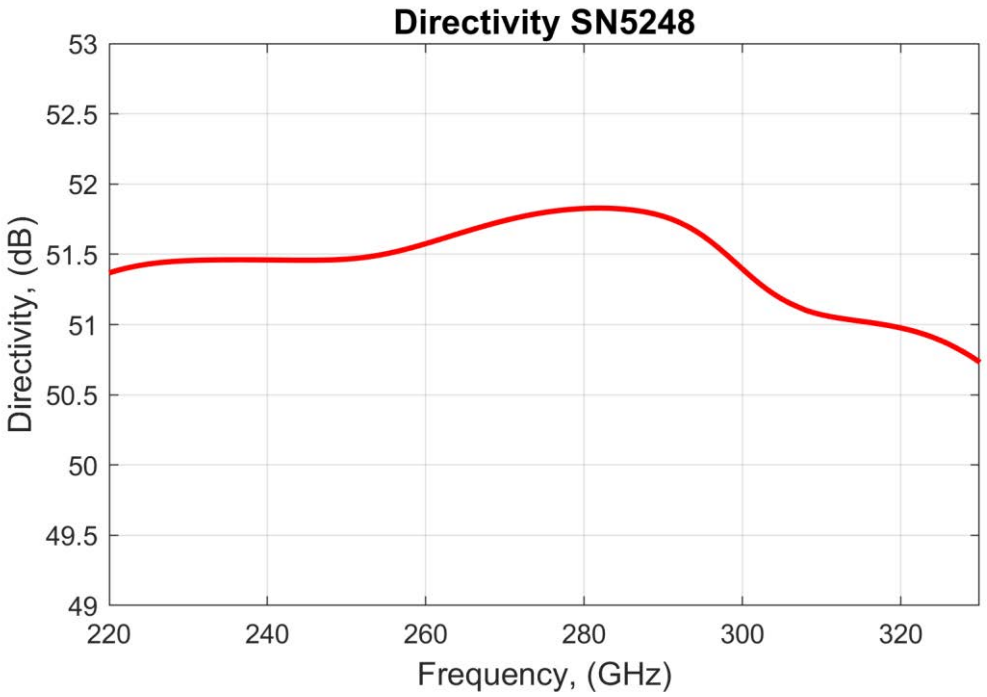

Figure 20. Measured directivity of prototype 2.

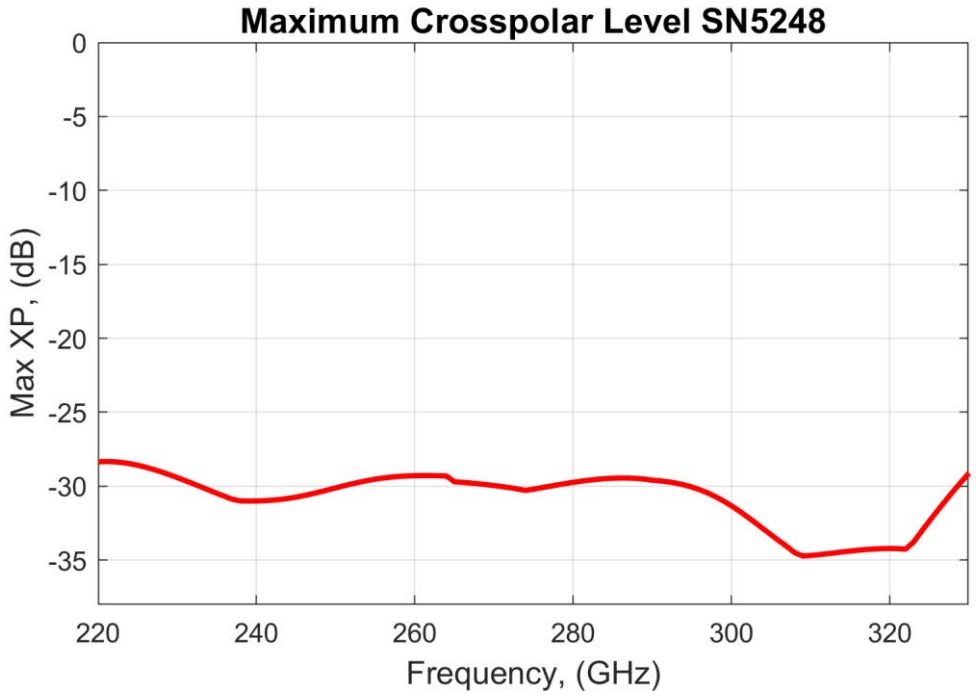

Figure 21. Max. measured crosspolar level of prototype 2.

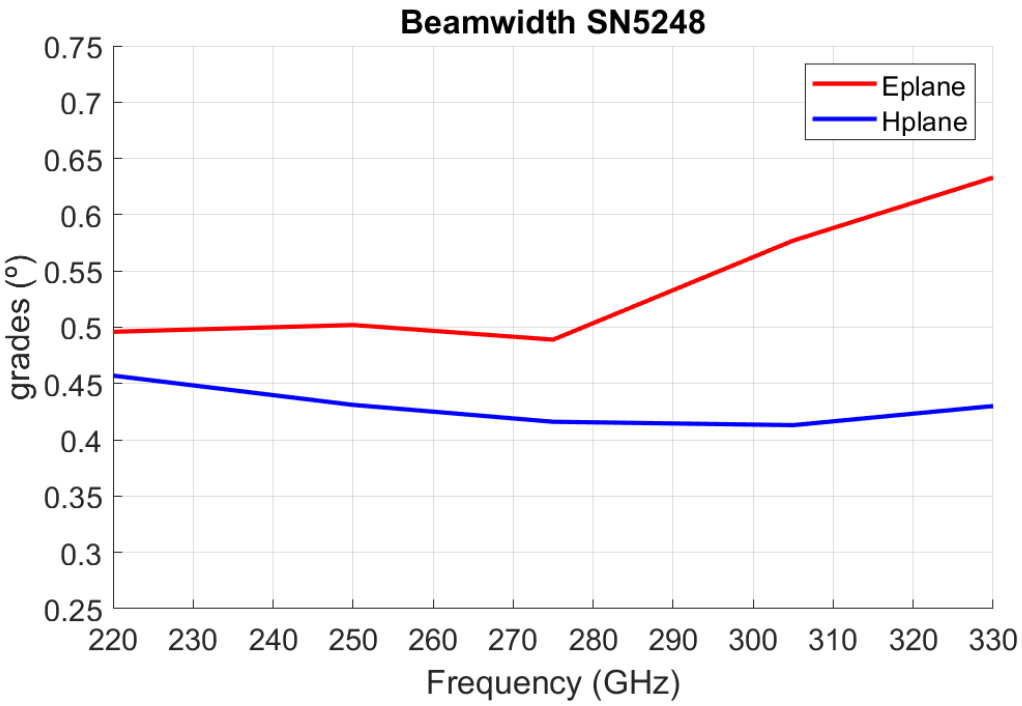

Figure 22. Beamwidth measured of prototype 2.

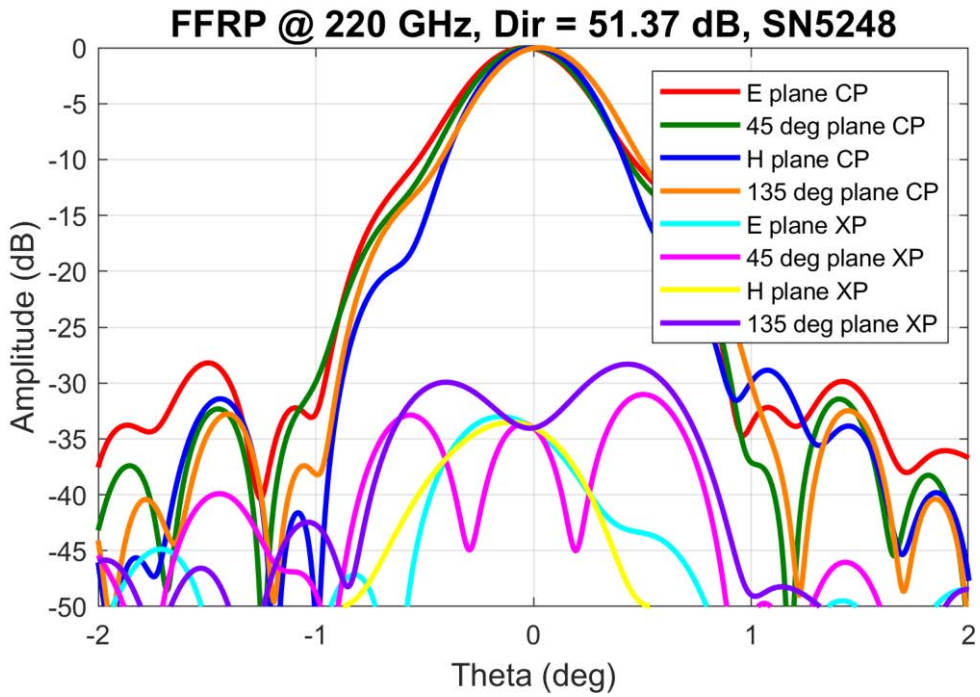

Figure 23. Measured far field radiation pattern at 220 GHz of prototype 2.

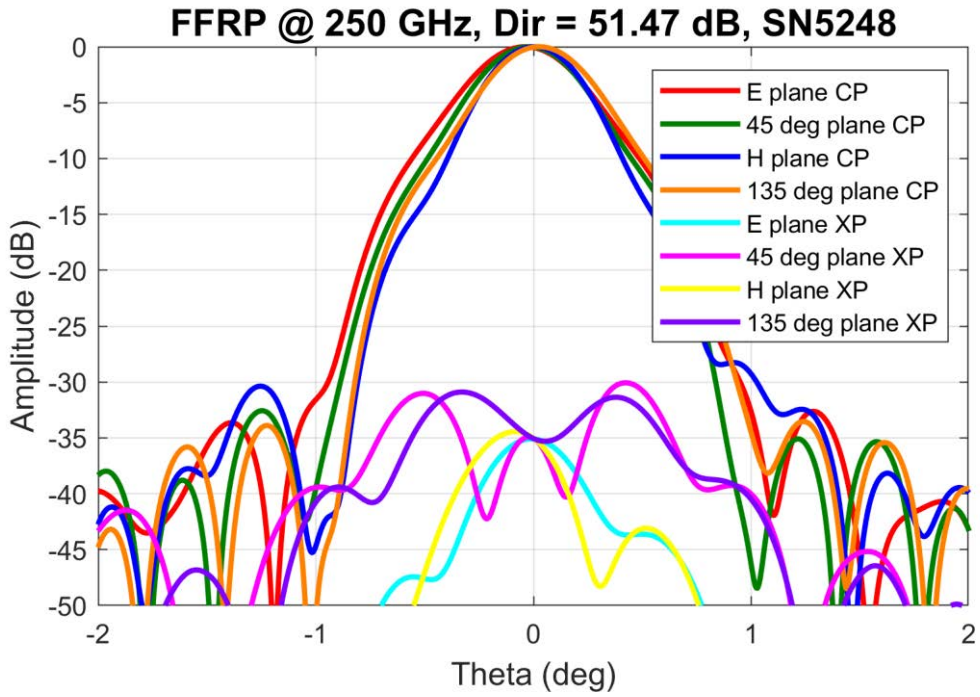

Figure 24. Measured far field radiation pattern at 250 GHz of prototype 1.

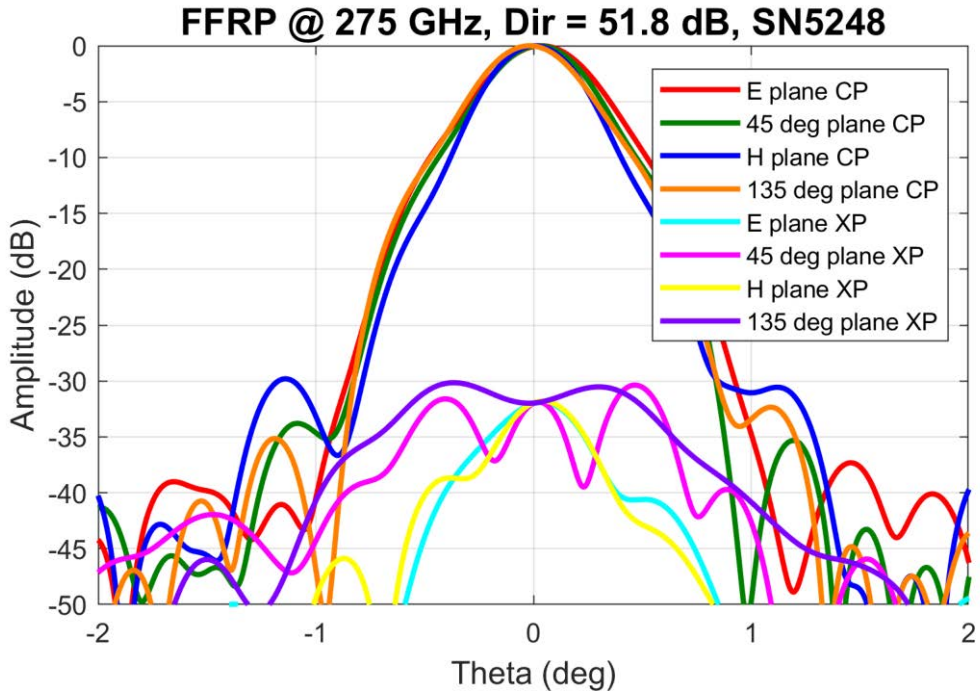

Figure 25. Measured far field radiation pattern at 275 GHz of prototype 2.

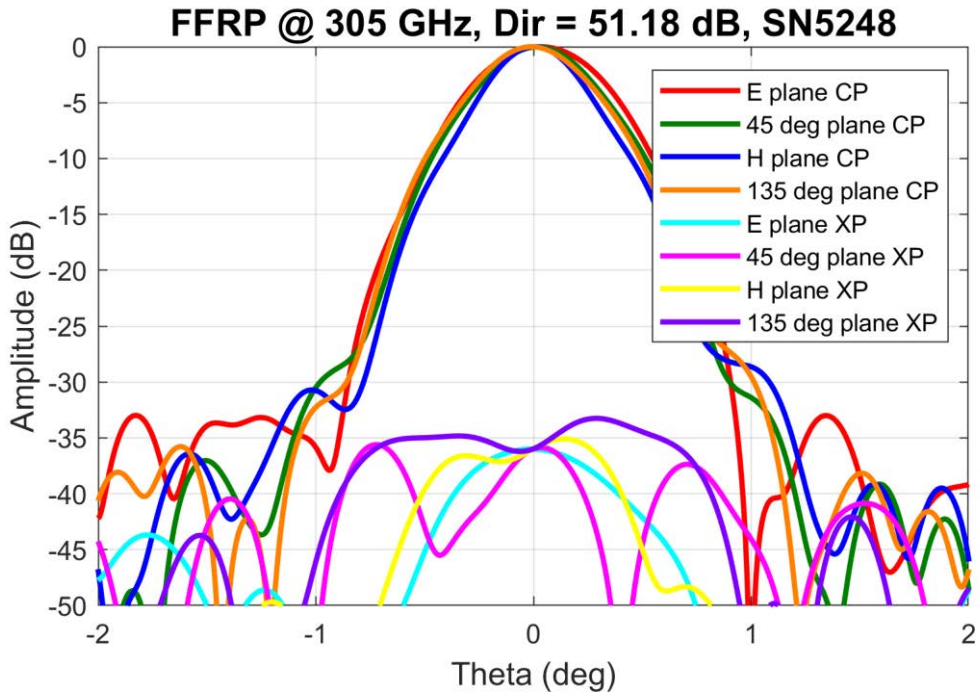

Figure 26. Measured far field radiation pattern at 305 GHz of prototype 2.

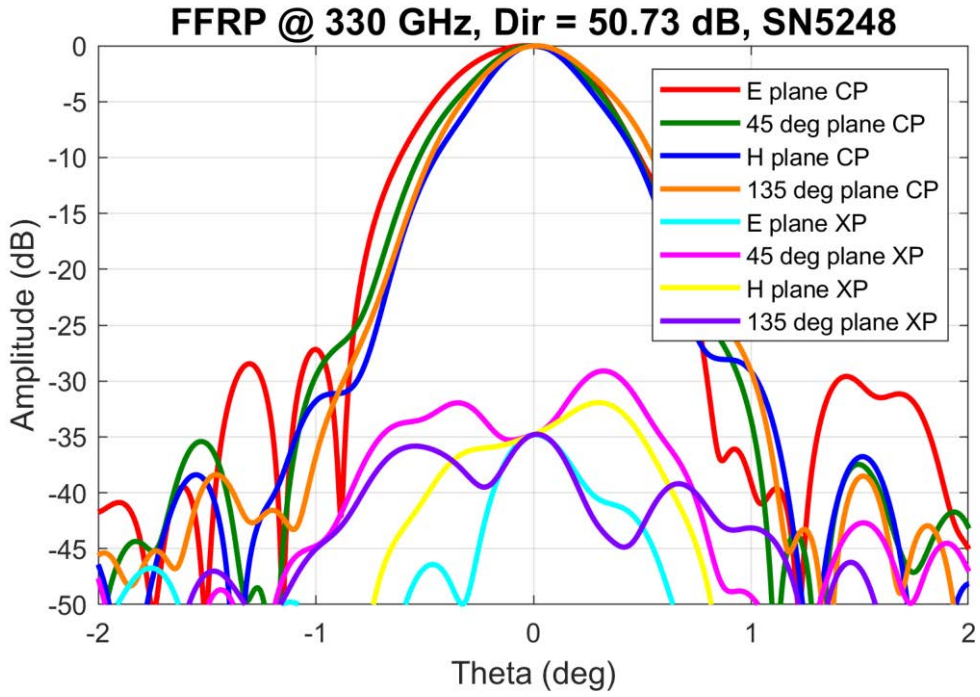

Figure 27. Measured far field radiation pattern at 330 GHz of prototype 2.

The measurement results are highly satisfactory and reflect the good performance of both prototypes. More specifically, in relation to the defined KPIs, the following conclusions can be drawn:

- The return losses are good, as seen in Figures 10 and 19, where the S11 value remains below -10 dB throughout the entire band of interest. The radiated power of the antenna relative to the delivered power is sufficient.
- The directivity exceeds 50 dB across the entire band for both prototypes. Prototype 1 exhibits higher directivity, approximately 1.5 dB at its peak value. Despite being the same manufactured model, this clearly demonstrates that small manufacturing inaccuracies can affect the final performance. At 300 GHz, where the wavelength is 1 mm, manufacturing tolerances must be very small, on the order of tens to a hundred microns.
- Similarly, the beamwidth is less than 0.5 degrees in Prototype 1 and less than 0.65 degrees in Prototype 2. These beamwidth values allow for the calculation of the illumination area for use in the PoCs.
- Although not considered in the KPIs, the cross-polarization component was also measured, showing very good performance in both prototypes, remaining below -25 dB.
- The radiation pattern graphs at different frequencies demonstrate proper beam shaping for all axes in copolar orientation (CP) and cross-polar rejection (XP). The sidelobes range between -25 dB and -30 dB (or better) at all frequencies. In some cases, the -30 dB value defined in the KPI is not fully met, but this is not a critical factor that would prevent the correct operation of the antennas.

The following table shows a summary of the results regarding the KPIs.

Table 4. KPIs requirements and measured results.

KPI	Requirement	Measured Result
Return loss	< -10 dB	< -10 dB at some frequencies < -15 dB at most frequencies
Directivity	> 45 dBi	> 50.5 dBi
Mean beamwidth	< 2 degrees	< 0.65 degrees
Losses	< 1.5 dB	Not measured but < 1.0 dB according to simulation
Sidelobe level	< -30 dB	< -25 dB in some frequencies < -30 dB in most frequencies

3 Development of beam steering antennas

This section describes the development of two different models of beam steering antennas that will be also used as components of the demonstration hardware in the PoC. Two different models have been designed and manufactured to test two different approaches. Since the fabrication of this type of antenna is a significant challenge, the strategy is to design two different options to ensure the highest reliability for the final implementation in the PoC.

3.1 Motivation

Beam-steering antennas [8] are especially significant in the PoC because of their unparalleled flexibility in directing radio waves within industrial environments, a capability that is especially crucial for high-frequency communications where signal attenuation and interference pose significant challenges. By dynamically steering the beam, these antennas concentrate energy toward specific devices or areas, ensuring optimal signal delivery while minimizing power wastage and maximizing system efficiency—an essential factor in energy-sensitive industrial settings.

Industrial facilities, often characterized by complex layouts with metallic structures that cause severe multipath interference, benefit from beamforming techniques that adapt the beam pattern in real time to mitigate the adverse effects of reflections and obstacles. This enhanced signal quality leads to higher data throughput and more reliable communication links, particularly important for high-frequency signals that are susceptible to environmental disruptions. In manufacturing plants and warehouses, where consistent connectivity is critical to support automation and real-time monitoring, beam-steering antennas ensure robust communication even in dynamically changing conditions. Their rapid adaptability reduces system downtime, boosting overall operational productivity, while their ability to selectively focus the beam decreases interference among multiple concurrently operating devices. This selective focus enables dense channel reuse, enhancing spectral efficiency and making it possible to deploy more devices without compromising performance—a key requirement for the dense network architectures of modern Industry 4.0 applications.

Additionally, beam-steering facilitates efficient spatial multiplexing, further increasing network capacity and reliability through advanced control algorithms that continually adjust the beam direction for optimal real-time performance. Industrial systems benefit from improved quality of service due to these dynamic adjustments, and the targeted transmission not only enhances communication but also contributes to significant energy savings, leading to lower operational costs. Seamlessly integrating with existing systems, beam-steering technology offers a scalable solution that ensures communication networks remain resilient in the face of environmental and structural challenges. Continuous innovation in beamforming techniques promises even greater improvements in future industrial deployments, making beam-steering antennas pivotal in enhancing the reliability, efficiency, and overall performance of industrial communication networks, and marking a significant advancement towards smarter, more resilient, and energy-efficient industrial systems.

The next table shows the set of KPIs introduced in [3].

Table 5. Beam steering antennas KPIs.

Parameter	Condition and value	Remarks
Return loss	< -10 dB	Across the full operation bandwidth (220 – 330 GHz)
Directivity	> 14 dBi	Maximum value
Steering angle	20 to 50 degrees	
Losses	< 2 dB	

3.2 Design strategy

Beam steering in this type of antenna is achieved through the radiation of multiple elements, where the electromagnetic wave radiated by each element has a different phase. This individual phase control can be implemented in various ways, but it mainly falls into two categories: passive or active beamforming. In this case, passive antennas have been chosen due to their lower complexity, as they do not require active components, reduced latency, wider bandwidth, and lower power consumption.

The design idea for the proposed antennas for the PoC is that, depending on the emission frequency, the phase of each element varies, and therefore the direction of maximum radiation changes. In this way, beam pointing is achieved by varying the frequency. Similar to high-gain antennas, there are many different approaches to passive antennas that exhibit beam-steering behaviour. Two different configurations have been chosen and have been designed: a slotted leaky wave antenna and an antenna with phase delay lines. Both antennas have their pros and cons, which will be described below.

3.3 Leaky Wave Antenna.

3.3.1 Leaky Wave Antenna. Design and simulation results.

Leaky wave antennas (LWAs) are a class of antennas that utilize the principle of guided waves leaking energy continuously along the length of the structure to produce radiation [9] [10]. These antennas typically consist of a waveguide or transmission line with periodic discontinuities or apertures, allowing energy to leak out gradually. This controlled leakage results in a radiation pattern that can be steered by varying the operating frequency, making LWAs highly suitable for applications requiring beam steering or scanning capabilities without mechanical movement. LWAs offer advantages such as simple structure, wide bandwidth, and high directivity, making them popular in modern wireless communication systems.

This design proposed here is a type of LWA that uses a waveguide (WG) structure with slots to control the direction of the radiated electromagnetic waves. The antenna design typically consists of a rectangular waveguide with a series of narrow slots along its length that allow it to leak power gradually. By properly controlling the phasing and amplitude of the signals fed to each slot, the antenna can create constructive interference in the desired direction and suppress radiation in other directions.

The slotted WG LWA design is shown in Figure 28. It has been designed to operate from 220 GHz to 320 GHz and sweep from 0°to 45°, with gain values between 20 dBi and 26 dBi.

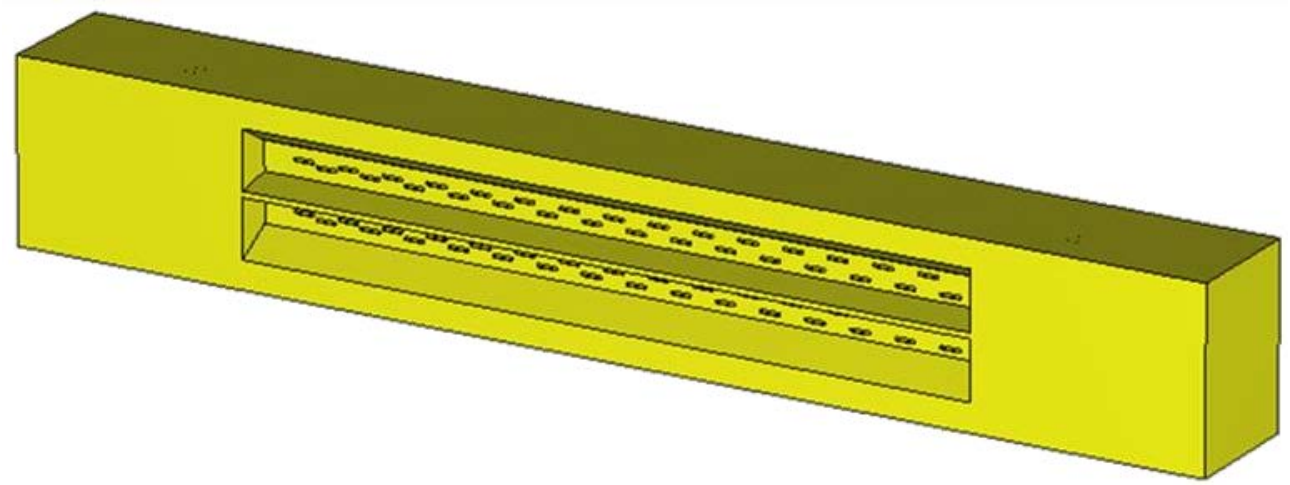

Figure 28. Slotted WG LWA schematic.

Initially it consisted of a single slotted waveguide with a line of slots longitudinally arranged in a V-shape distribution, as it can be seen in the upper slots row in the picture above. To increase the antenna's gain, it was decided to add a second parallel waveguide, rather than increasing the number of slots. To feed both waveguides, it was needed to design a power divider at both ends of the waveguides (Figure 29), as well as the optimization of the separation between the WGs and inner dimensions of the power divider, in addition to other critical parameters as slots period and dimensions. The input is a standard WR-3.4 rectangular waveguide.

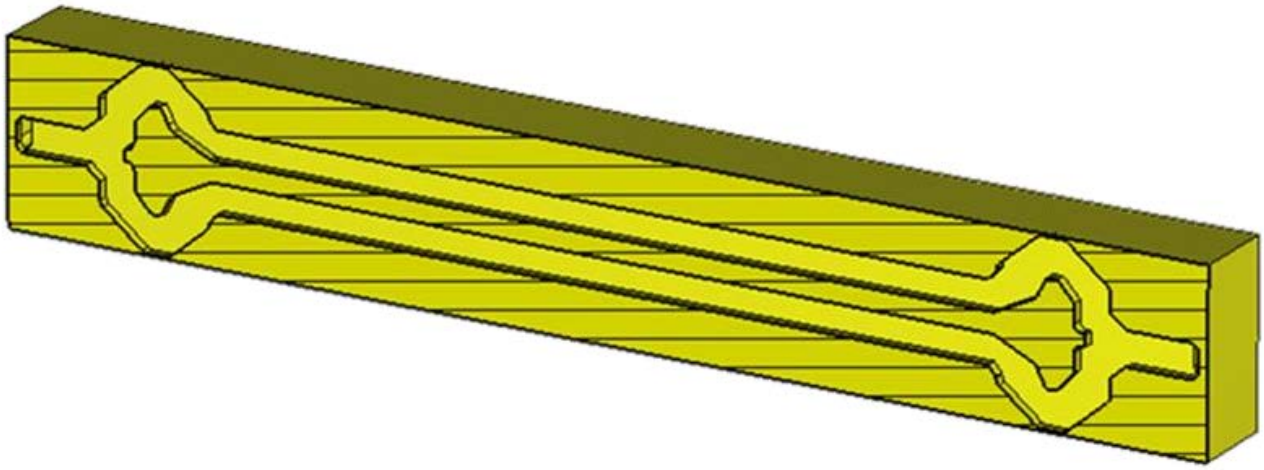

Figure 29. Antenna's inner guide and power splitters schematic

The inclusion of the second waveguide increased the gain but resulted in higher side lobes in the vertical plane (transversal to the antenna's length). So, a longitudinal tapered horn was attached to the aperture side (slotted face) of each waveguide, Figure 30. This enhanced the gain and reduced the undesired lobes.

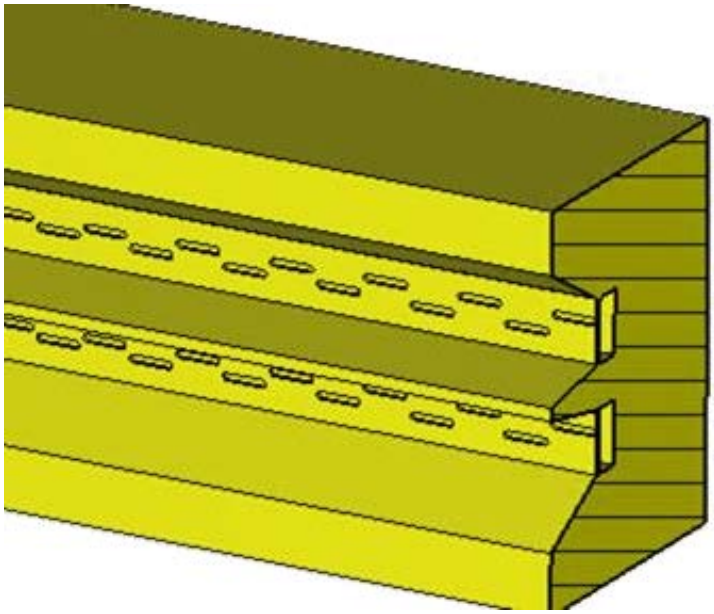

Figure 30. Detail of attached longitudinal tapered horns.

Lastly, to make the connection of the antenna to the modems feasible, an elbow was included at both ends of the power splitters to orient the feeding port towards the orthogonal (rear) direction, Figure 31. It is worth noting that this antenna has two ports. One is the feeding port and the other is a port that should be impedance matched. The option selected is to use a commercial load at the end to avoid any reflection to the slots part.

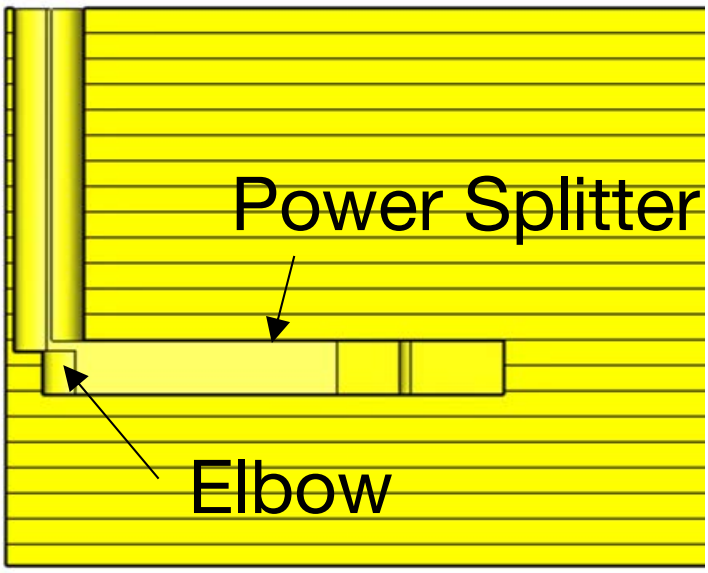

Figure 31. Detail of elbow attached to power splitter, side view.

The design and optimization of this antenna were carried out in CST. The antenna is well-matched, as shown in Figure 32, where the S11 is displayed and the values are below -10 dB across the entire bandwidth.

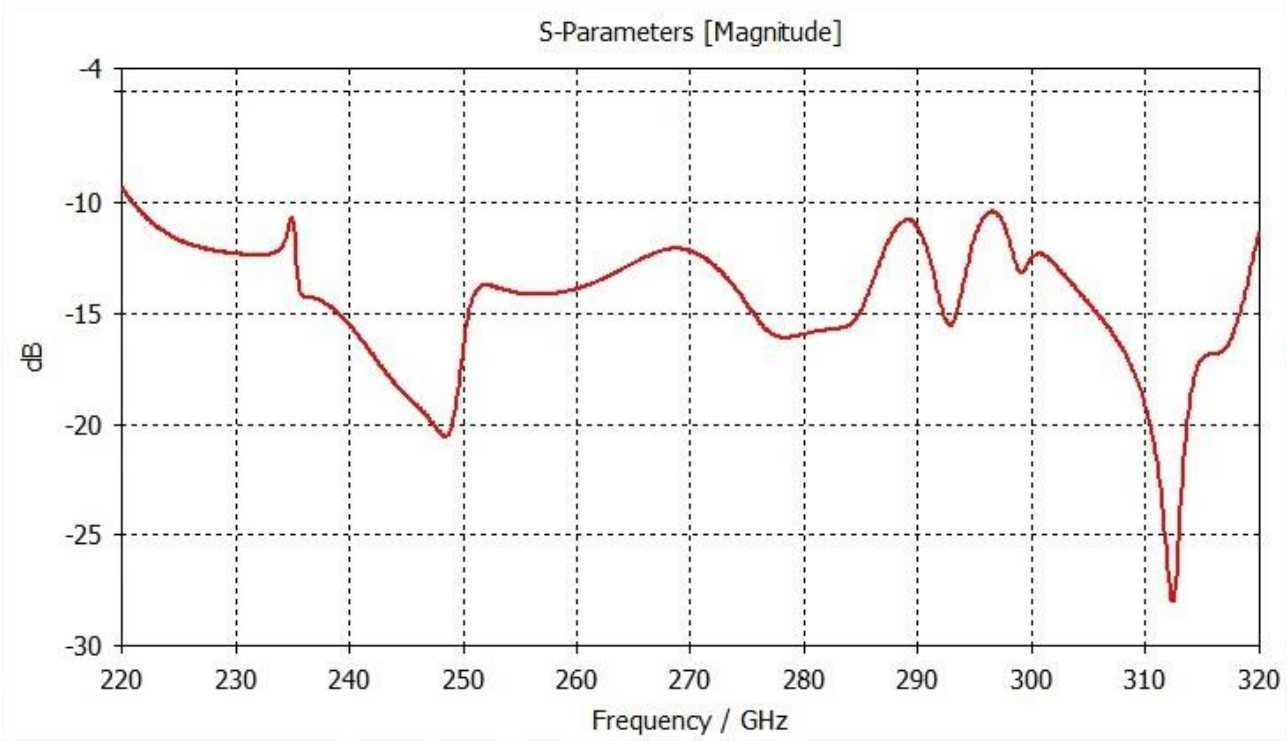

Figure 32. S11 of the leaky wave antenna.

The φ = 0° radiation diagram cuts are shown in Figure 33, while Figure 34 displays the farfield radiation pattern in 3D. As observed, the beam is steered from almost broadside to θ = -45° when the frequency is progressively changed from f = 300 GHz to f = 220 GHz. The gain decreases steadily with frequency from 25 dBi at 315 GHz to 20 dBi at 220 GHz. Hardly any sidelobes appear. Only at the lower frequency, a lobe appears at 45 degrees approximately.

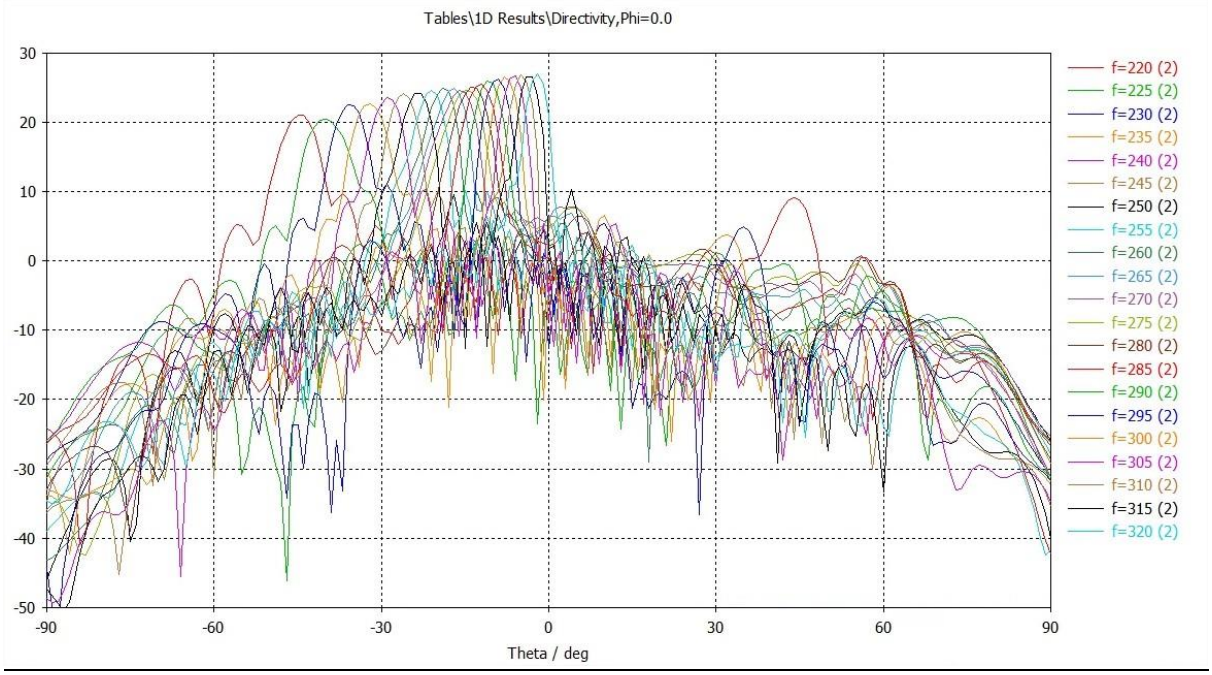

Figure 33. Radiation diagram cuts at φ = 0deg.

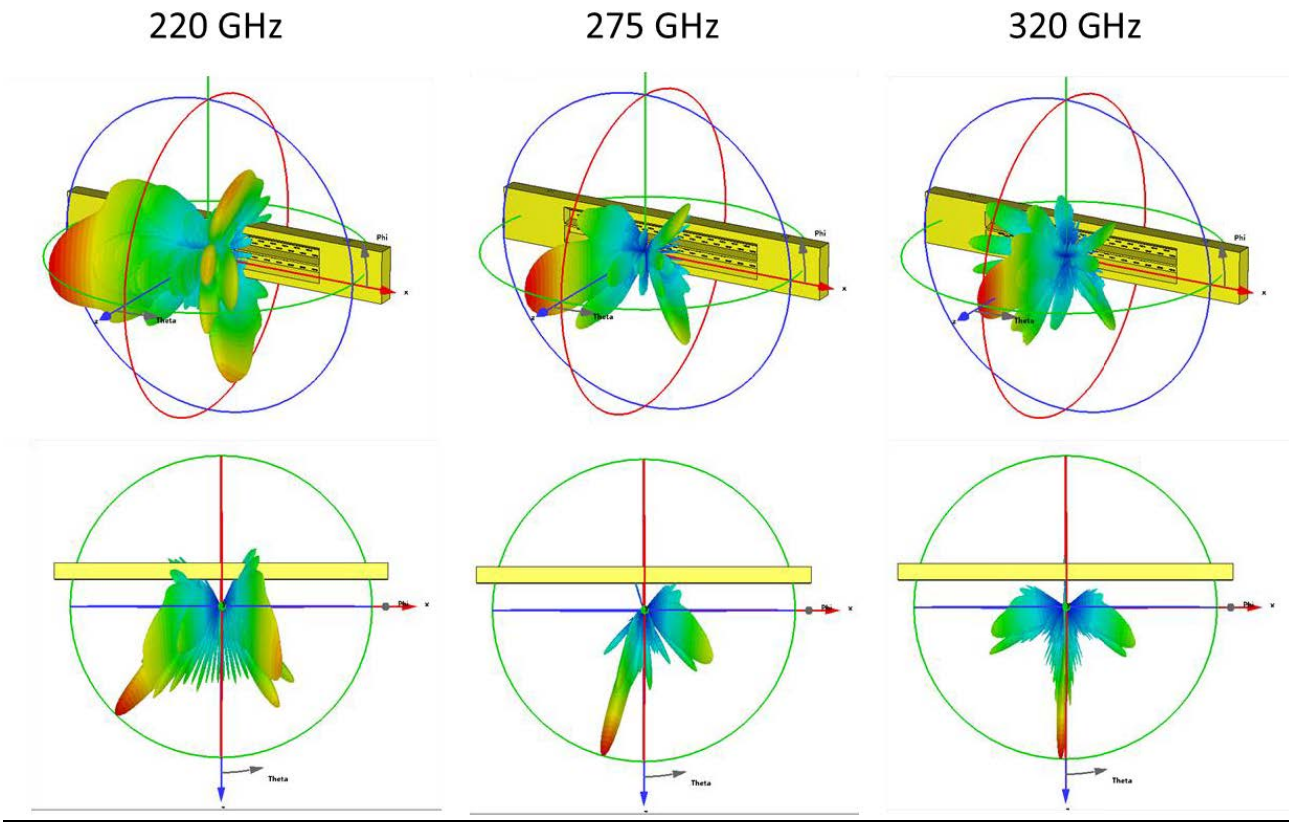

Figure 34. 3D farfield radiation pattern at different frequencies.

3.3.2 Leaky Wave Antenna. Mechanical design and fabricated prototype.

Once the simulation design is completed, the mechanical design is carried out. The antenna is highly complex, and its overall structure has been designed and manufactured in multiple parts.

1. The bottom part contains two standard WR3.4 flanges. One corresponds to the input waveguide, through which power is injected, while the other flange corresponds to the port where the non-radiated power from the slots must be absorbed. In this case, a matched load will be connected to this second port. Leaving it unconnected would cause undesired power reflections back into the antenna.
2. The middle section consists of the elbow, the power splitter and the channels of the two waveguides.
3. The front part includes the radiation slots and the small horn-shaped aperture of each of the two waveguides.

All parts are assembled and aligned using screws and alignment pins. The total size of the antenna is 50.36 mm × 24.6 mm × 12.55 mm. Figure 35 shows the 3D mechanical model of the antenna from both sides.

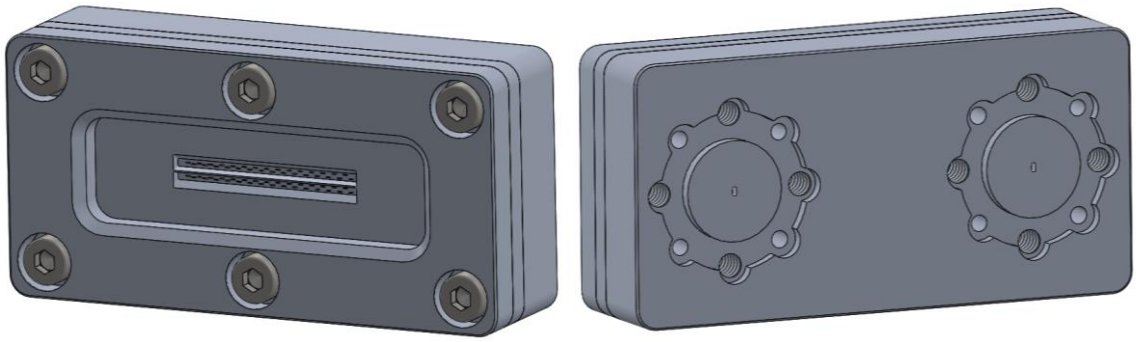

Figure 35. 3D mechanical model of the LWA.

The entire antenna is made of aluminum. The main manufacturing technique used is traditional milling. For smaller areas such as the flanges or bends, electron beam forming is used. The most challenging part to manufacture is the radiation slots. Laser-based techniques have been employed for their fabrication. Figure 36 shows a microscope photo a one of the fabricated slots and its measured length. The design length is 500 um and the measure shows a tolerance of just one micron.

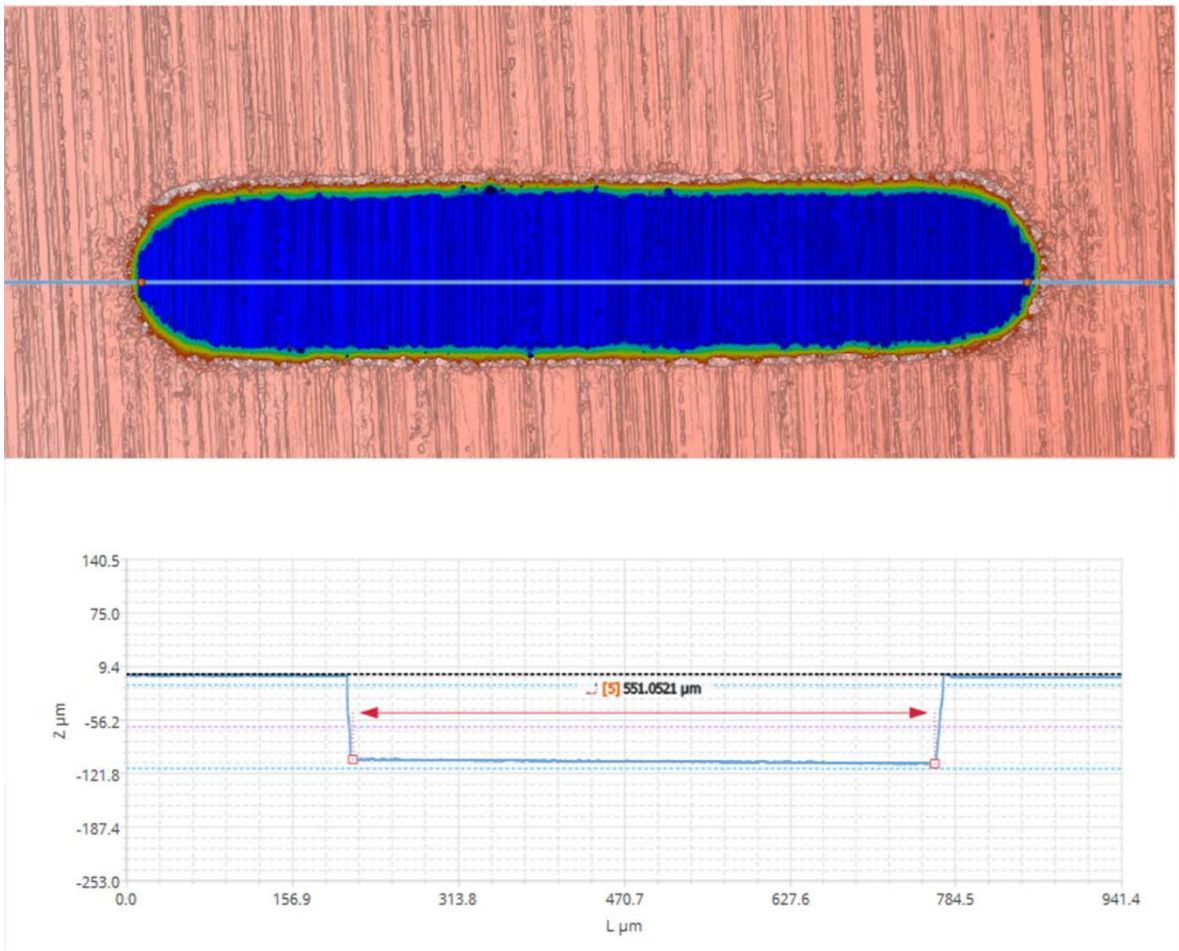

Figure 36. Fabricated slot (top) and measured length (bottom)

Figure 37 shows various detailed photographs of some of the other manufactured parts of the final prototype.

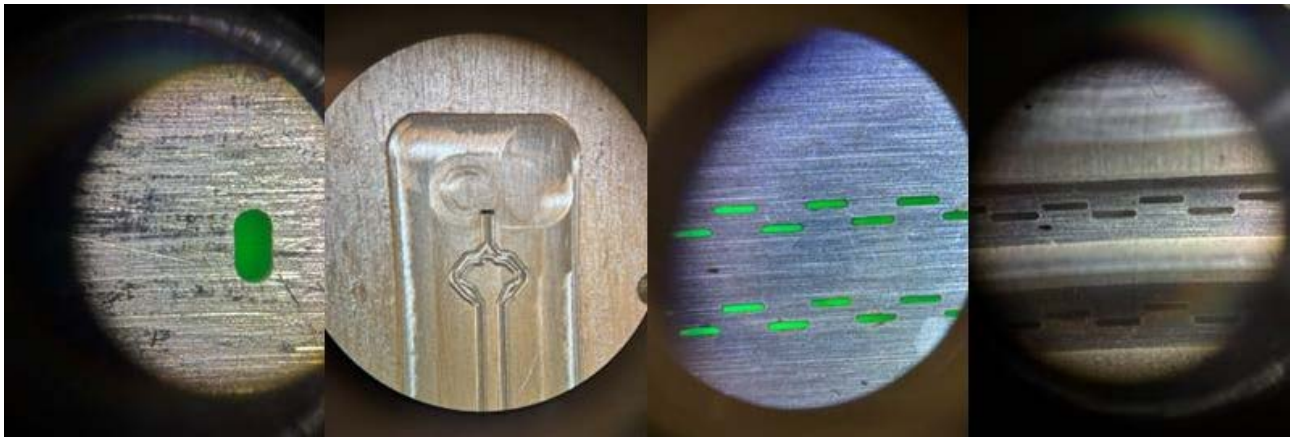

Figure 37. Detailed photographs of the LWA.

The final appearance of the prototype is shown in Figure 38. The photos also include a straight-section waveguide and the matched load at each of the standard ports.

Figure 38. Final prototype of the LWA.

3.3.3 Leaky Wave Antenna. Validation results.

3.3.3.1 Proposed method for Leaky Wave Antenna characterization

The proposed method used to characterize the LWA can be divided in two parts: First, a horn conical antenna working in the WR3.4 band is characterized using a testbed on a 220-325 GHz Vector Network Analyzer (VNA) and the gain, depicted in Figure 39, is calculated from S_{21} measurement and the usual Friis equation.

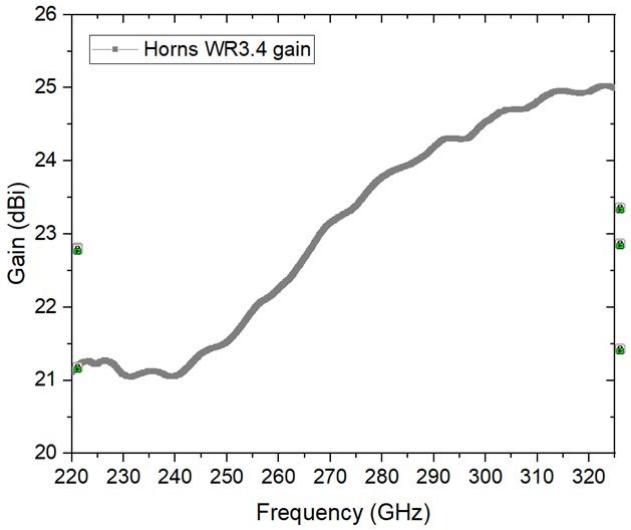

Figure 39. Horn antenna gain (Horn input is a WR3.4 waveguide).

Second, a radiation pattern testbed (Figure 40) is used is used to obtain the actual gain of the LWA. Here, a reference transmitter is used as an input for the antenna under test (AUT). On the left of Figure 40, we see the electronic part based on a ×18 multiplier used to feed the waveguide flange of the LWA. In front of Figure 40, the 3D robot system is shown. The receiver is coupled to the reference horn antenna, which was characterized by 220-325 VNA prior to this experiment. Then, by moving the 3D robot system on a ½ sphere (one move is displayed in yellow in Figure 40) around the AUT, the gain of the AUT is obtained by the horn antenna thanks to the fixed distance (200 mm) and the calibrated receiver gain.

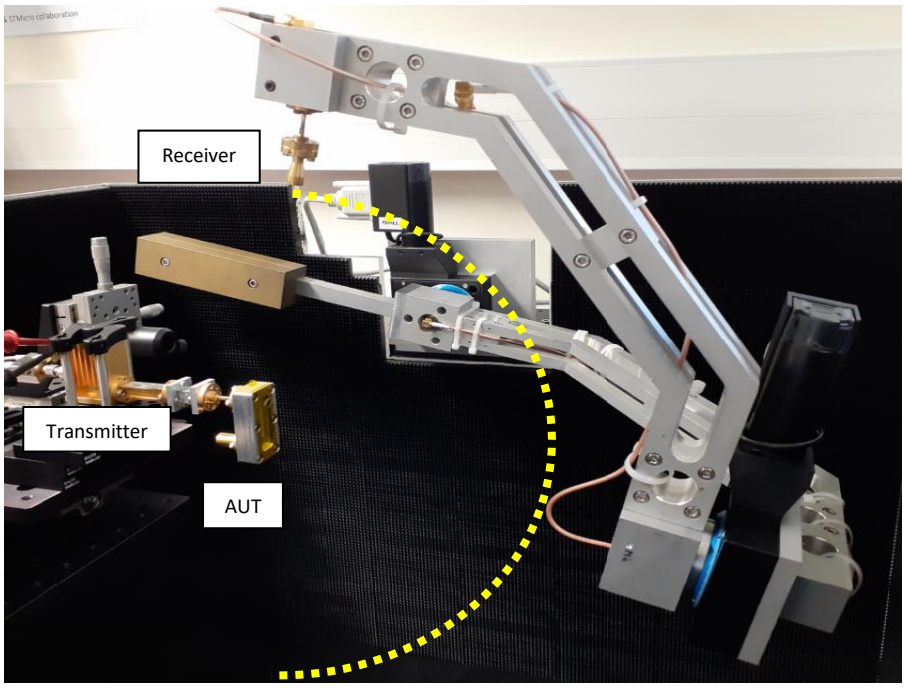

Figure 40. Proposed testbed for antenna characterization. One trajectory for one angle of the ½ sphere measurement pattern is shown in yellow dashed line.

3.3.3.2 Pattern of the designed Leaky Wave Antenna

As described in previous sections, the steering capability of the LWA onto the 220-320 GHz frequency band has been simulated and is shown in Figure 33. By the proposed testbed previously described, the 2D LWA normalized gain pattern is measured for several frequencies in the $\varphi = 0°$ direction. The results are compared with simulations in Figure 41. As it is seen on the figure, the steering capability of the LWA between 50° and 90° is clearly validated for the tested frequencies. Above 320 GHz a sidelobe is observed due to this frequency is above the operational band.

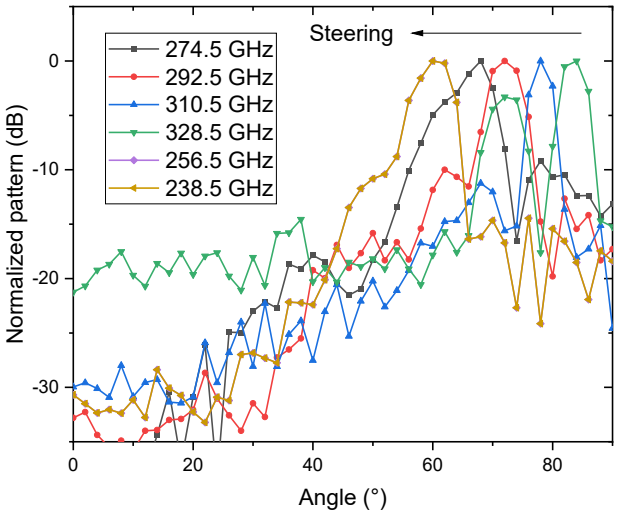

Figure 41. Normalized gain of Leaky Wave Antenna pattern ($\varphi = 0°$) measured.

A 3D scan of the LWA pattern at 274.5 GHz has also been done and is shown in Figure 42. Even though the z-axis is in linear scale, it is clear that the signal coming from the LWA is narrow and almost only directed around 70° even though for low signal, the signal is large.

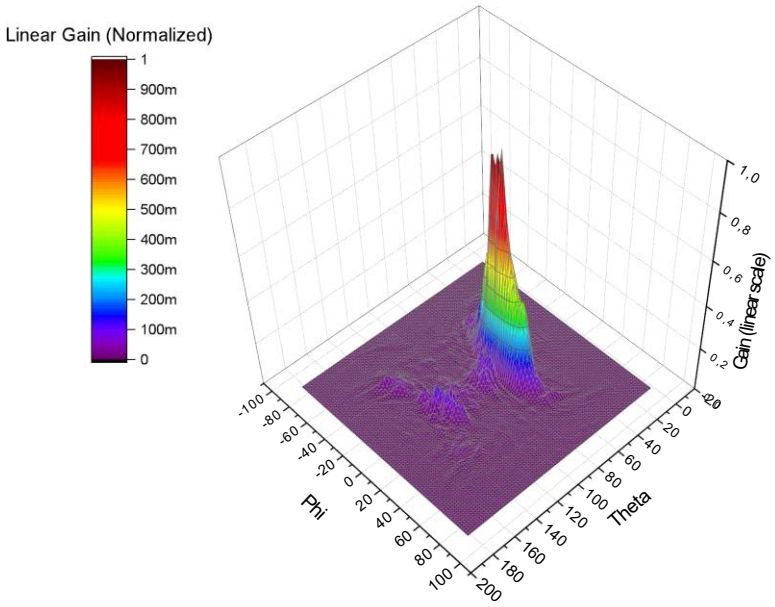

Figure 42. 3D scan of the LWA pattern (in linear scale) at 274.5 GHz.

3.3.3.3 Steering performance

In Figure 43, the steering performance of the LWA is shown. As can be seen from this figure, the agreement of the simulated and measured behavior is reached. However, there is a rough 7~8% shift between simulations and measurements in terms of achieved angle of radiation. It means that for a fixed angle, the LWA radiated the signal with a higher frequency as the one expected from simulations, but the frequency steering of LWA is demonstrated. It doesn't prevent to use it, as the range 260-320 GHz is covered. Looking on the the slopes of both curves in the frequency band of main importance, an averaged 0.34°/GHz steering performance is obtained.

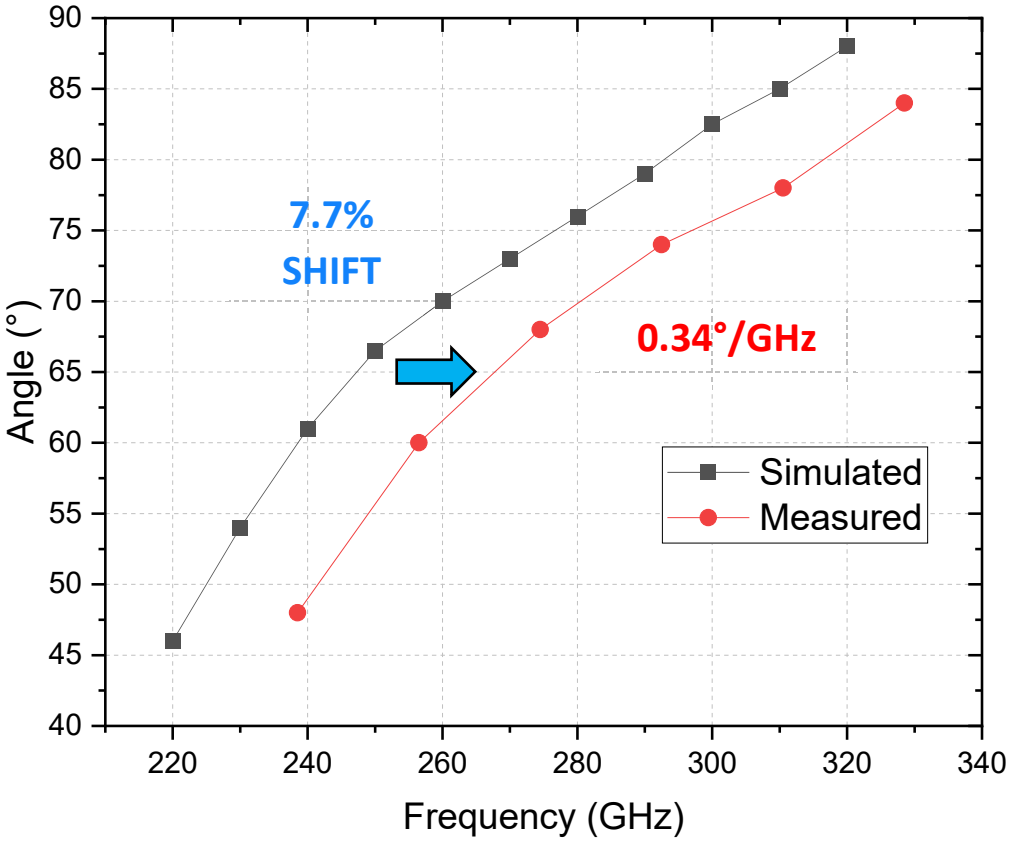

Figure 43. Measured steering performance of the LWA (in red) and comparison with simulations (in black).

3.3.3.4 Measured gain of the designed Leaky Wave Antenna

As explained at the beginning of this section, the actual LWA gain can be retrieved by comparing the relative gain between the LWA and the Rx horn antenna directly measured from the proposed testbed and the actual horn antenna gain measured by VNA method. Figure 44 is then obtained by this technique. First, and as it is shown on the figure, a 13 dB difference is seen between measurements and simulations. The reduced gain is caused by the impact of sidelobes and possibly by RF losses in the structure. Compared with simulations, the LWA bandwidth is a bit lower, but a 50 GHz bandwidth on which the LWA gain is higher than 10 dB is clearly seen in the measurements.

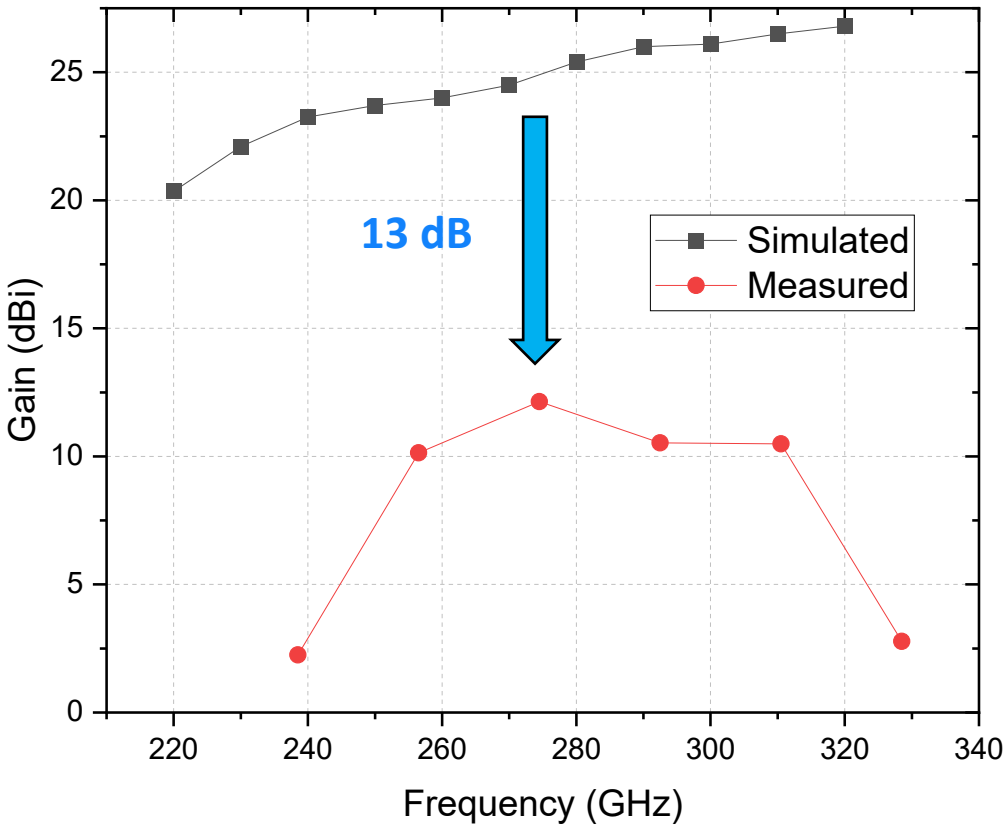

Figure 44. Measured Leaky Wave Antenna gain (in red) and comparison with simulations (in black).

3.3.3.5 Measured return loss of the designed Leaky Wave Antenna

The return loss is also measured with the VNA by means of a one-port calibration and covering the antenna output with absorber. The obtained result is depicted in Figure 45.

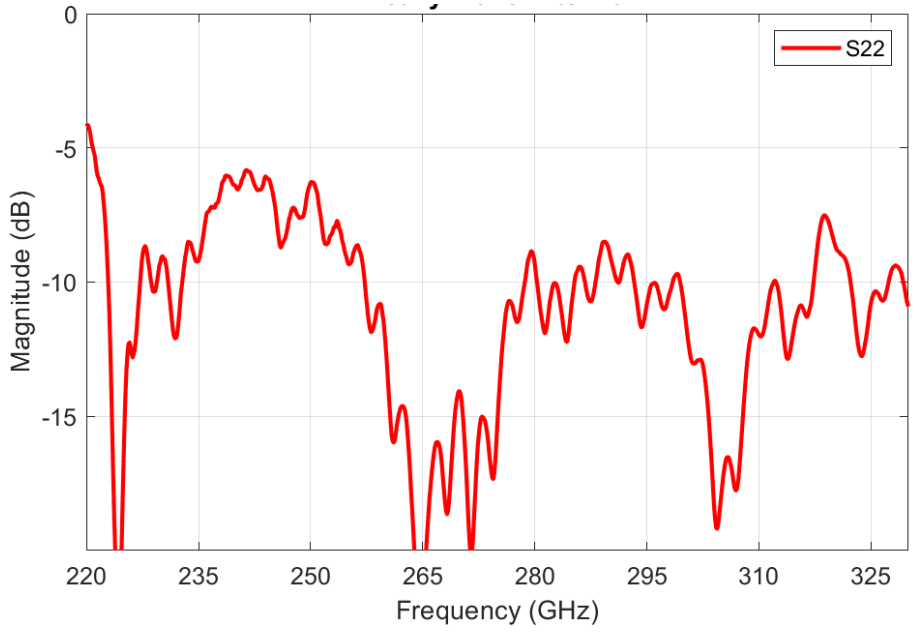

Figure 45. Measured Leaky Wave Antenna return loss.

It can be noticed that at lower frequencies the adaptation is worse where at 240 GHz the return loss is -6 dB. However, above 255 GHz, the return loss is below -8 dB where several sub-frequency bands well below -10 dB.

The following table shows a summary of the results regarding the KPIs.

Table 6. KPIs requirements and measured results of LWA.

KPI	Requirement	Measured Result – Leaky Wave Antenna
Return loss	< -10 dB	< -6 dB, full operational bandwidth < -8 dB, 220 – 235, 255 – 320 GHz
Directivity	> 14 dBi	> 20 dBi (according to gain diagram)
Steering angle	20 to 50 degrees	37.4 degrees
Losses	< 2 dB	13 dB

The antenna performance, based on the proposed KPIs, can be considered acceptable. The total realized gain must be included in the power budget for the dimensioning in proof-of-concept testing. The source of the high losses is currently being investigated to mitigate this effect in future manufacturing.

3.4 Phase Delay Line Antenna.

3.4.1 Phase Delay Line Antenna. Design and simulation results.

The design idea behind the Phase Delay Line Antenna (PDLA) is to achieve individual phase shifts for each element by introducing dividers and delay lines. In this way, the input signal is split and arrives at each radiating element with a different phase. This phase is controlled by the total final length of each path. For each frequency, a summed wave is transmitted from the interference generated by each individual element, resulting in a specific radiation pattern and, therefore, a desired beam pointing. The final performance of the antenna depends on several factors, but three are crucial for our use case: the number of individual elements, their shape, and the spacing between them. These parameters determine the total pointing angle, directivity, and unwanted radiation at other angles, respectively.

The designed antenna is divided into two blocks. The first is the feed network with the delay lines, represented in Figure 46. The input, which is a standard WR-3.4 waveguide, is divided into three levels to have 8 individual waveguides at the output. Figure 39 shows a view of this feed network design. The power dividers are symmetrical, and the network is designed so that at 300 GHz, the phase differences between the output ports are multiples of 360°, ensuring the antenna points to boresight at that frequency.

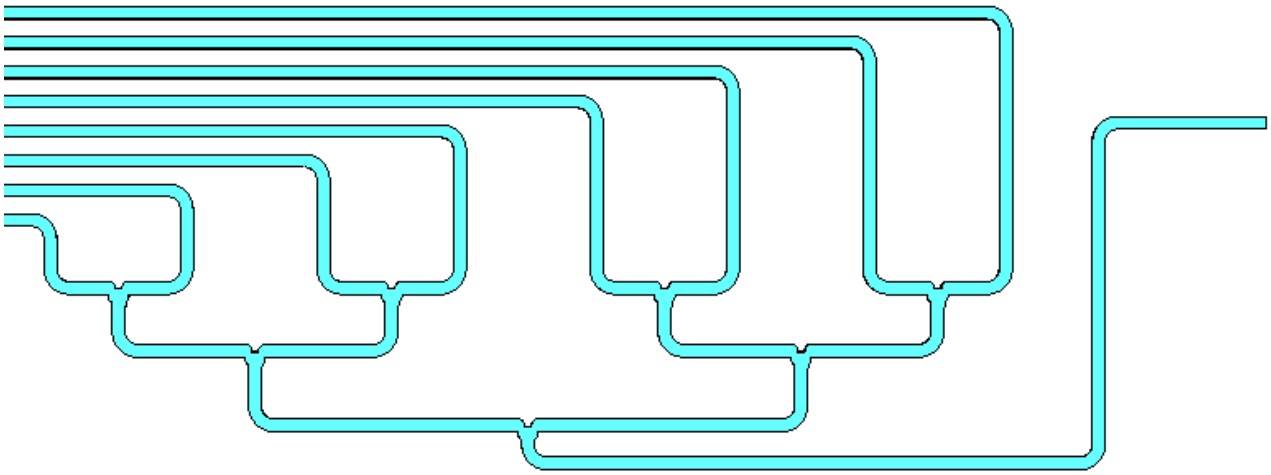

Figure 46. Feeding network.

At frequencies different from the central frequency, the wave does not arrive in phase at each output port, and a wave is generated that is the constructive sum of the phases at each port. The phase difference at each port is related to the radiation angle with the following formula:

$$\Delta\phi = \frac{2\pi}{\lambda} d \sin\theta$$

with $\Delta\phi$ the phase delay, λ the signal wavelength, d the port separation and θ de radiation angle.

The idea for the fabrication of this network is to manufacture it through conventional milling. Therefore, the smallest waveguide size cannot be less than 0.4 mm in width. This network would be manufactured in two pieces: a body and a cover. The cutting of these two pieces would be done in the E-plane to minimize losses in the assembly of the two parts. The initial path has been designed so that the input port is aligned with the boresight pointing direction of the output array.

To achieve the desired directivity of the antenna, the feeding network ends in a second block that adapts the output of each of the eight feeding waveguides as if it were a sectoral horn. Since the feeding network is cut in the E-plane, the sectoral horns will be in the H-plane. These horns are spaced more than $\lambda/2$ apart, which impacts the diffraction lobes. This limitation is imposed by the manufacturing conditions. Figure 47 shows a cross-sectional image of the complete antenna.

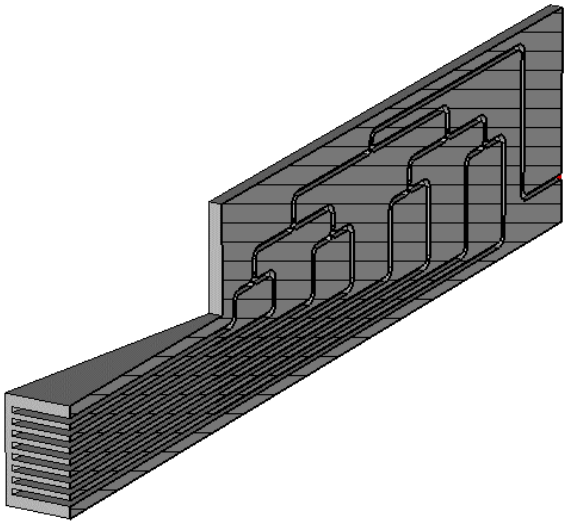

Figure 47. Cross-sectional view of the PDLA

The design and simulation of this antenna are carried out using CST. Figure 48 shows a sectional view of a part of the feeding network, where the magnitude and phase of the electric field can be observed, as well as its behavior in the power dividers. In Figure 49, the phase variation at the end of the lines for the band edges and the central frequency is illustrated.

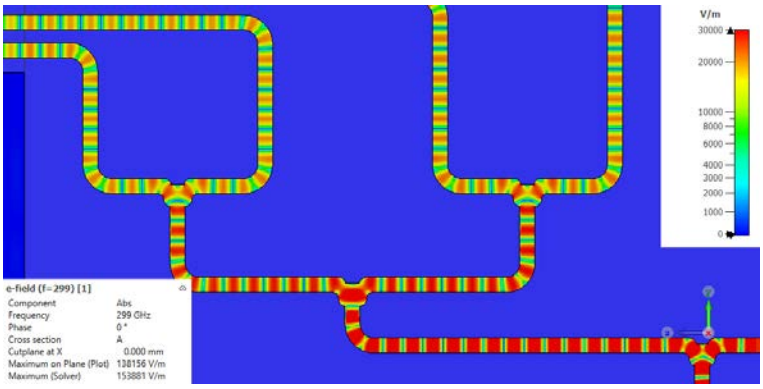

Figure 48. Cross sectional view of E-Field at the power splitters.

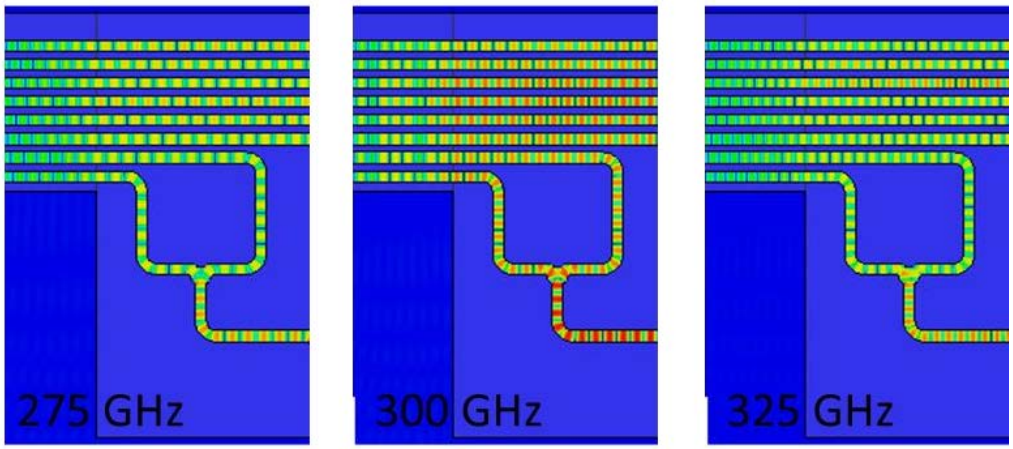

Figure 49. Cross sectional view of E-Field at the end of the lines at different frequencies.

This antenna has a narrower operational bandwidth compared to the LWA. While the LWA exhibits full matching from 220 to 330 GHz, the PDLA has approximately half the bandwidth at these frequencies. The operational bandwidth is not only related to impedance matching but also to the beam-steering capability, as will be seen later.

Figure 50 shows the return losses obtained in the simulation. A good impedance matching is observed, remaining below -10 dB across most of the target bandwidth from 275 to 300 GHz. It is worth noting that near the central frequency, some resonances appear, causing the S11 to reach up to -7 dB at a specific frequency.

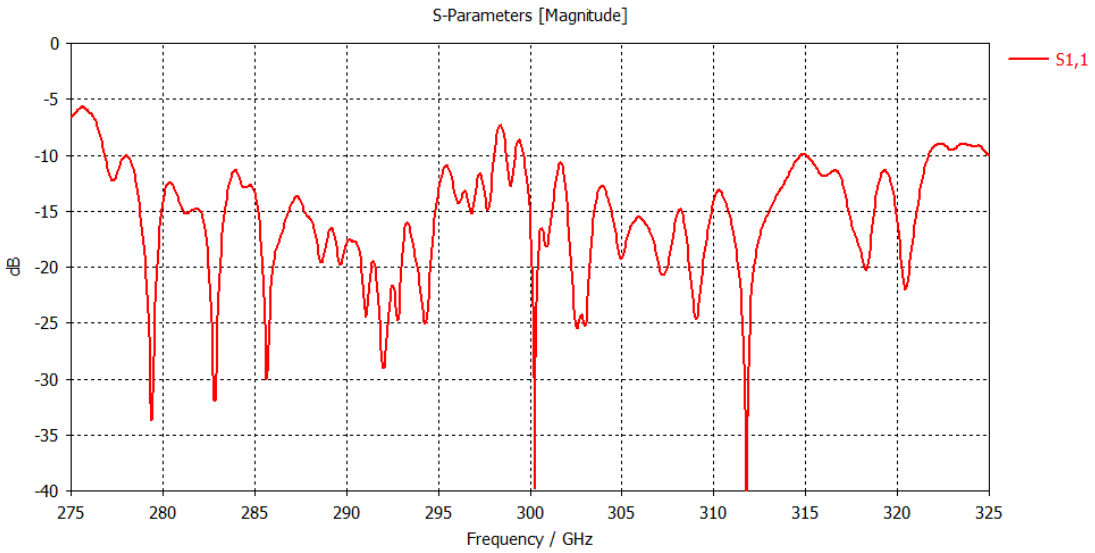

Figure 50. S11 of phase delay antenna

Regarding beam steering, Figure 51 shows the 3D far-field radiation pattern at various frequencies. At the central frequency of 300 GHz, where all apertures radiate in phase, the main lobe points at boresight. As the frequency decreases, the main lobe shifts to lower angles in the E-plane (the vertical axis in the figure), which is the axis where the apertures are located. Conversely, at higher frequencies, the beam shifts toward higher angles. The maximum beam steering achieved is ±50 degrees.

It can also be observed that as we move away from the central frequency, *grating lobes* become increasingly significant, nearly reaching the same size as the main lobe at the band edges. As previously mentioned, this is due to the fact that the spacing between the sectoral horns is greater than half a wavelength.

Additionally, the main lobe exhibits a beamwidth between 15 and 20 degrees, depending on the frequency, while remaining symmetric in both axes. The vertical array of apertures determines the beamwidth in that axis, whereas the length and opening angle of the sectoral horns define the horizontal beamwidth. The horns are designed to produce a symmetric main lobe.

Figure 52 and 53 shows the radiation pattern cuts at φ = 90° for all frequencies. In addition to the beam steering of the main lobe and the appearance of grating lobes, it can be observed that the maximum directivity remains fairly constant, around 20–22 dB across the entire band, except at the center, where it increases to 23–27 dB for frequencies between 295 and 305 GHz.

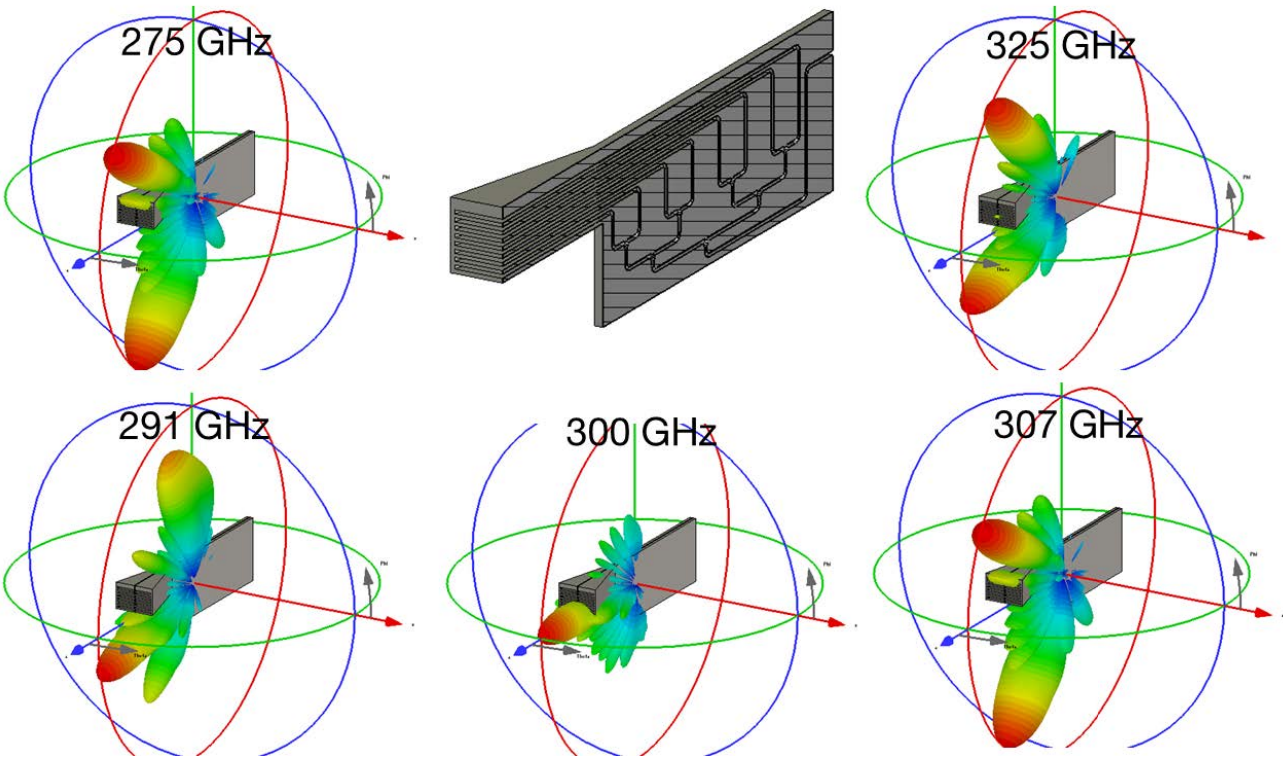

Figure 51. 3D farfield radiation pattern at different frequencies

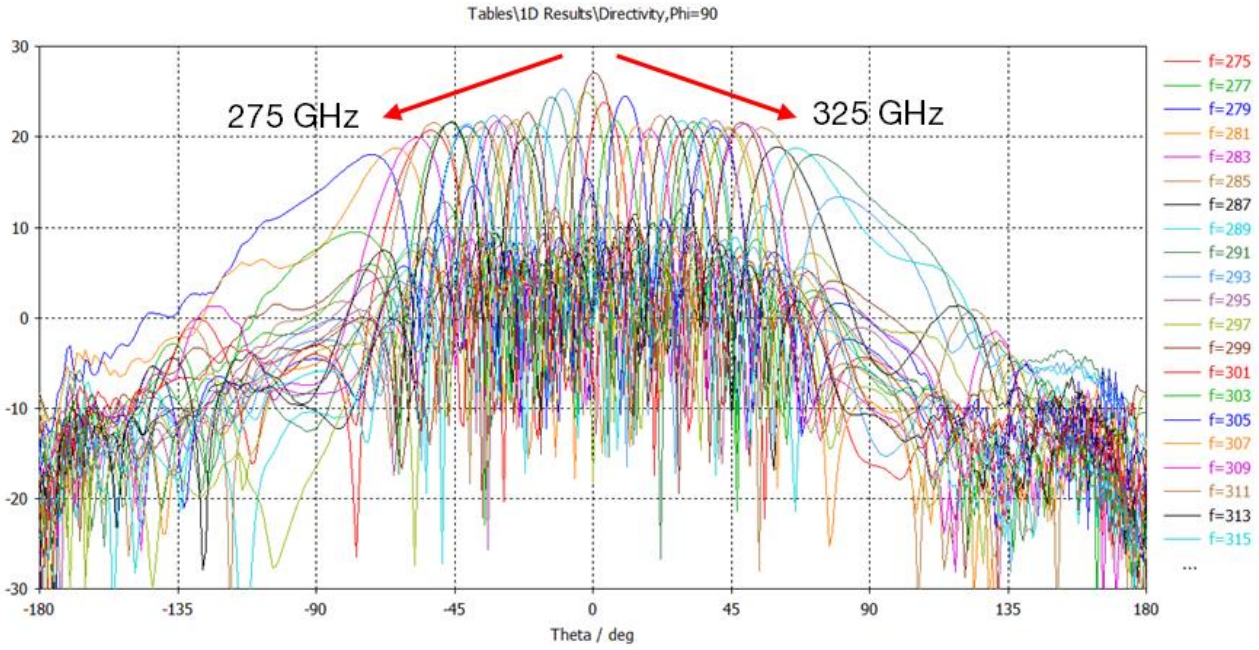

Figure 52. Radiation diagram cuts at φ = 90° for 275 to 325 GHz.

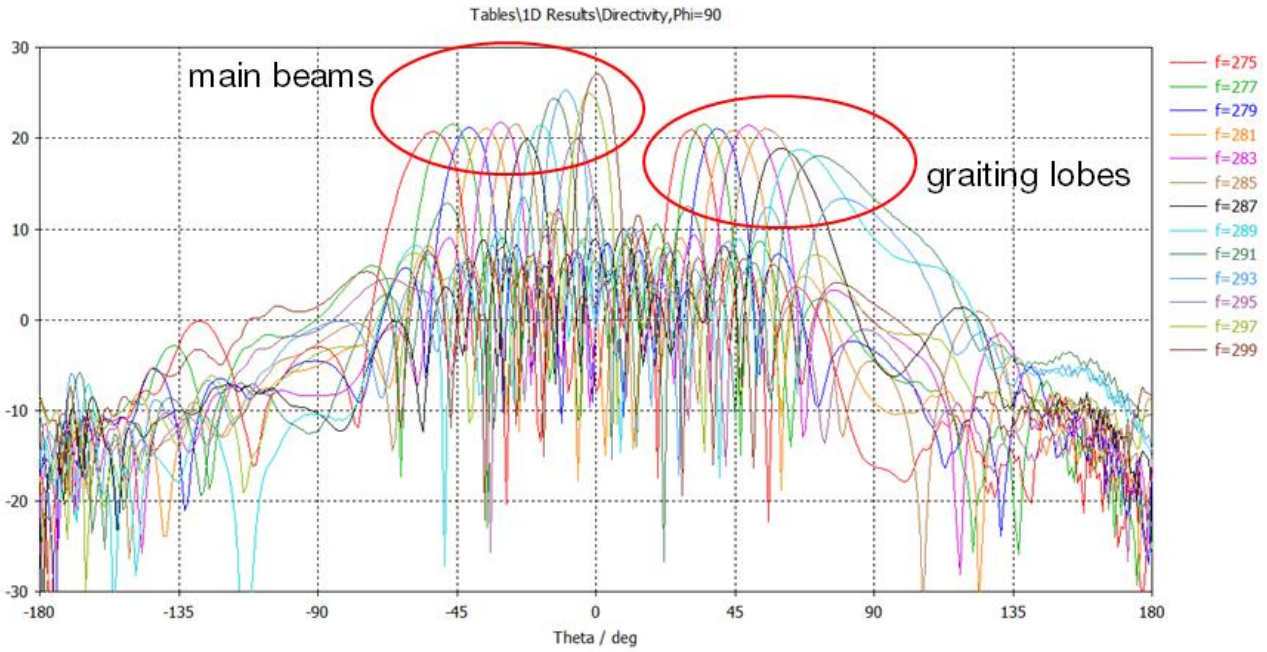

Figure 53. Radiation diagram cuts at φ = 90° for 275 to 299 GHz.

3.4.2 Phase Delay Line Antenna. Mechanical design and fabricated prototype.

The fabrication of this antenna is also a challenge due to its morphology and required manufacturing tolerances. When addressing the mechanical design, it is also decided to design it in multiple parts.

1. The first block contains the feeding network, from the standard WR3.4 flange to the termination of the eight waveguides.
2. The second block consists of the H-plane horns.

Both blocks are assembled together using screws and alignment pins to ensure proper alignment of all components. The antenna has overall dimensions of 76 mm × 38 mm × 28 mm. Figure 54 shows the mechanical model.

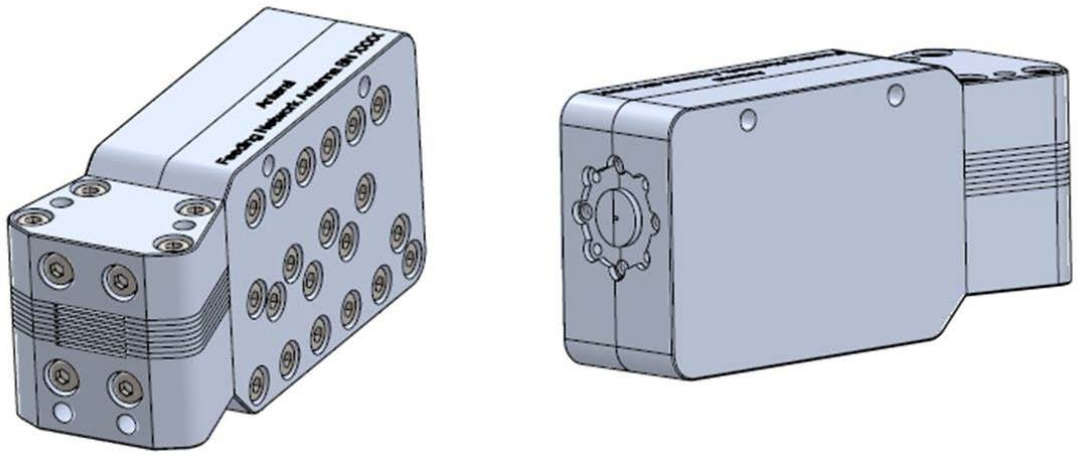

Figure 54. 3D mechanical model of the PDLA.

The entire antenna is made of aluminum. The main manufacturing technique used is traditional milling. For smaller areas such as the flanges or bends, electron beam forming is used. Figure 55 shows various detailed photographs of some of the manufactured parts of the final prototype.

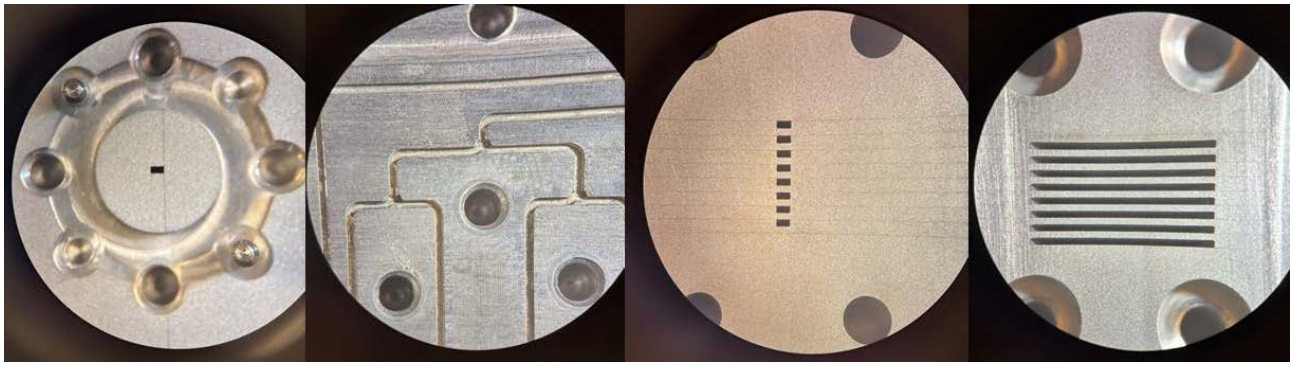

Figure 55. Detailed photographs of the PDLA.

The final appearance of the prototype is shown in Figure 56.

Figure 56. Final prototype of the PDLA

3.4.3 Phase Delay Line Antenna. Validation results.

The proposed testbed used to characterize the Phased Delay Line Antenna (PDLA) is the same as for LWA characterization. Thus, we are going directly into results discussion.

3.4.3.1 Pattern of the designed Phased Delay Line Antenna

In Figure 57, the normalized gain PDLA pattern in the $\varphi = 90°$ direction is shown. Several comments can be made about this figure. First, as for LWA, the steering performance of the antenna is also confirmed experimentally. Second, for several frequencies, the angular aperture of side lobes seems large and finally, the PDLA response behavior is highly frequency-dependent as it can be seen from the different patterns for different frequencies.

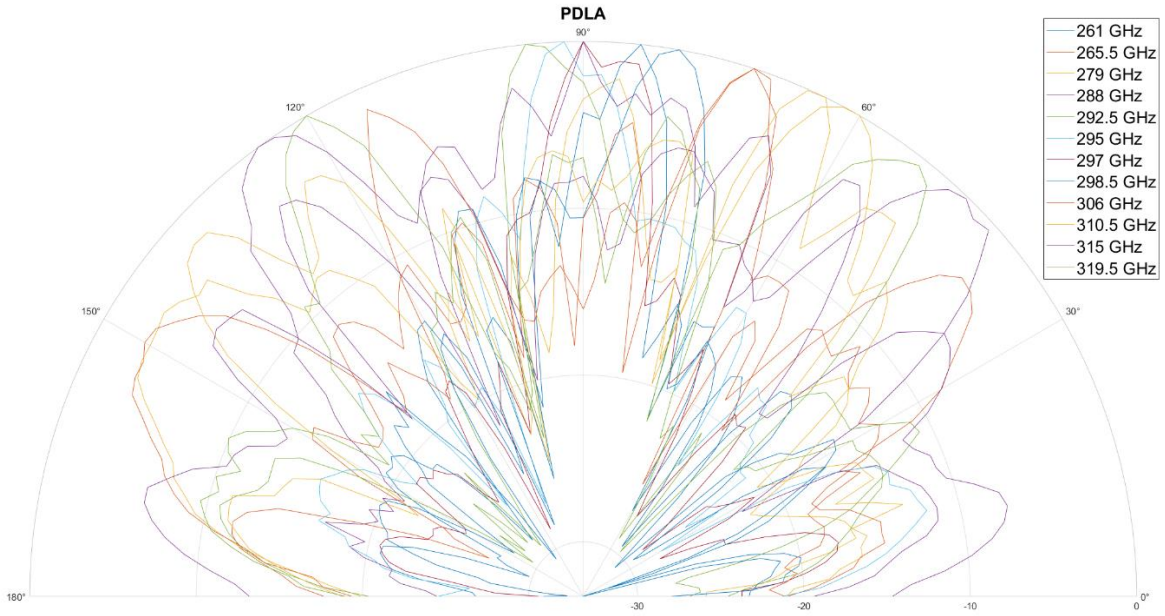

Figure 57. Normalized gain of Phased Delay Line Antenna pattern ($\varphi = 90°$) with respect to the steering angle for each measured frequency.

In the next figure, selected patterns are also shown for the PDLA:

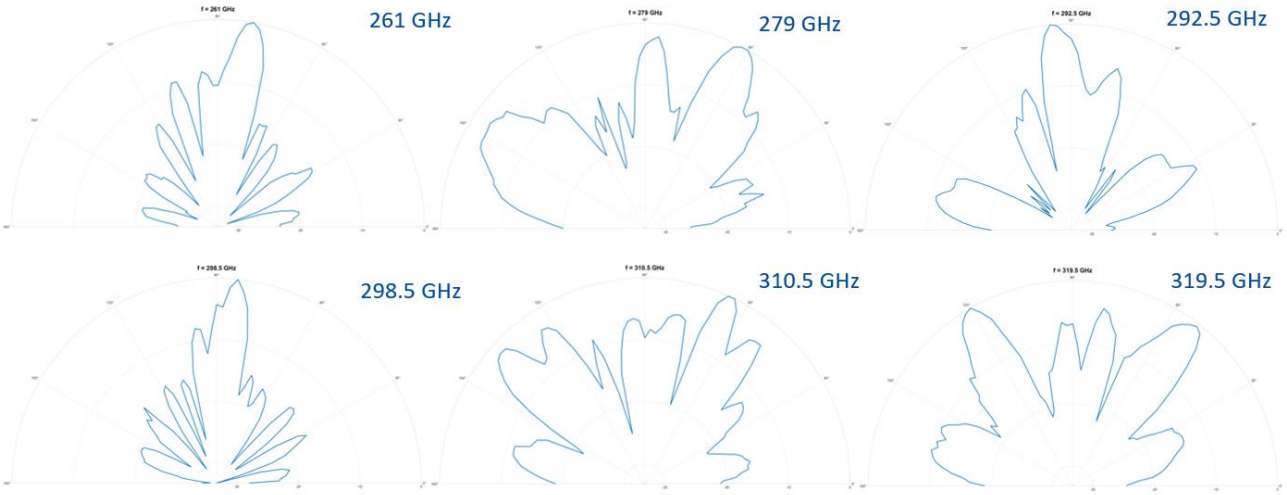

Figure 58. Normalized gain of Phased Delay Line Antenna pattern ($\varphi = 90°$) with respect to the frequency.

3.4.3.2 Steering performance

In Figure 59, the steering performance of the PDLA is shown. Compared to LWA, in the 280-310 GHz frequency band, measurements are really close to simulations with a very small (0.8%) shift (Red curve). Taking into account of few side lobes, it is still possible to keep the linear behavior of the steering versus frequency (green curve). This linear behavior can be linearly fitted to find a 2°/GHz slope steering performance which is also better than the 0.34°/GHz performance of the LWA.

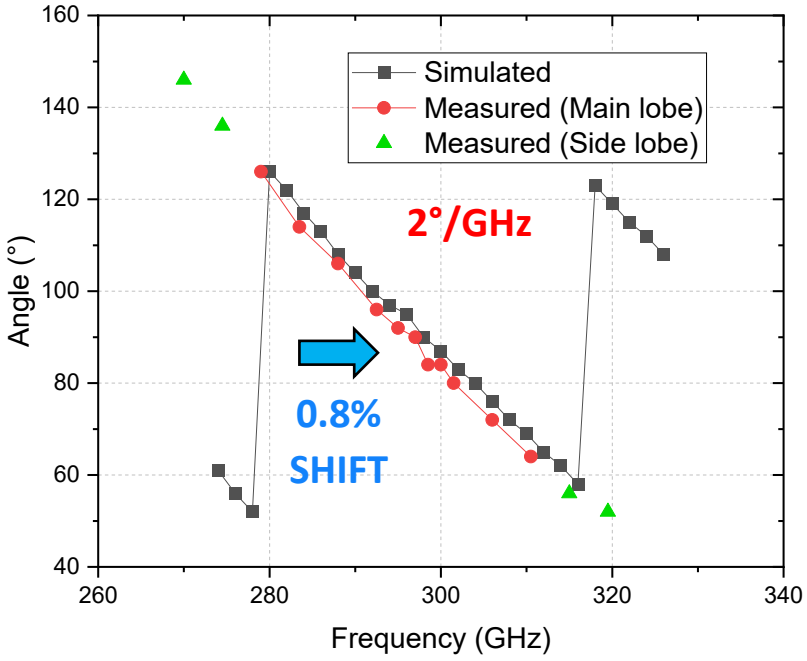

Figure 59. Measured steering performance of the PDLA by taking into account of main lobes (in red) or side lobes (in green) and comparison with simulations (in black).

3.4.3.3 Measured gain of the designed Phased Delay Line Antenna

As seen from Figure 60, the actual PDLA gain is retrieved by the same method as for the LWA gain. The gain in the $\varphi = 90°$ direction is not as high as in simulations, showing a 17 dB reduction, but the peak at 298 GHz is still well visible experimentally. Compared with LWA, in this case, a roughly 7 GHz bandwidth is found with an actual gain higher than 5 dB.

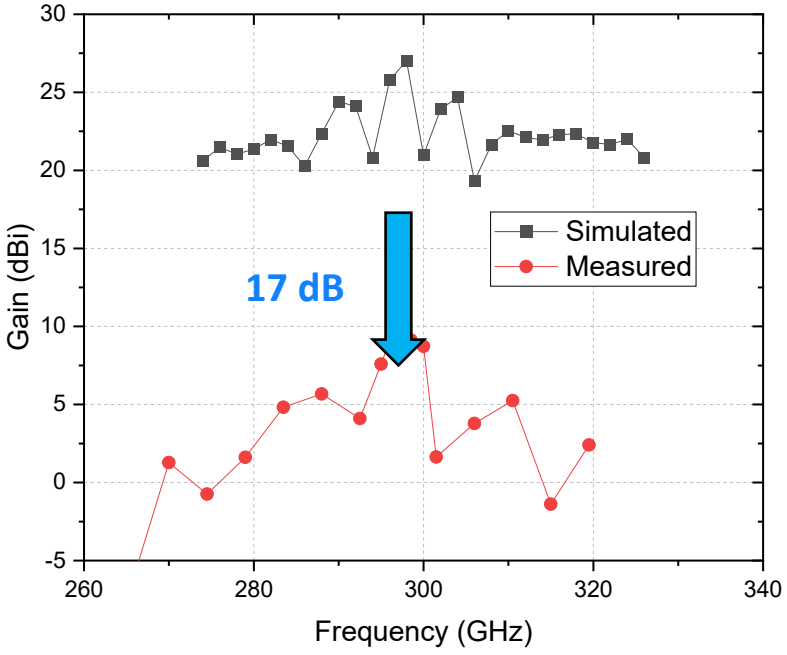

Figure 60. Measured Phased Delay Line Antenna gain (in red) and comparison with simulations (in black).

3.4.3.4 Measured return loss of the designed Phase Delay Line antenna

The return loss is also measured using the VNA via a one-port calibration, with the antenna output terminated by an absorber. The resultant data is depicted in Figure 61. The measurement results demonstrate a favourable return loss across the entire operational bandwidth, exhibiting values below -10 dB.

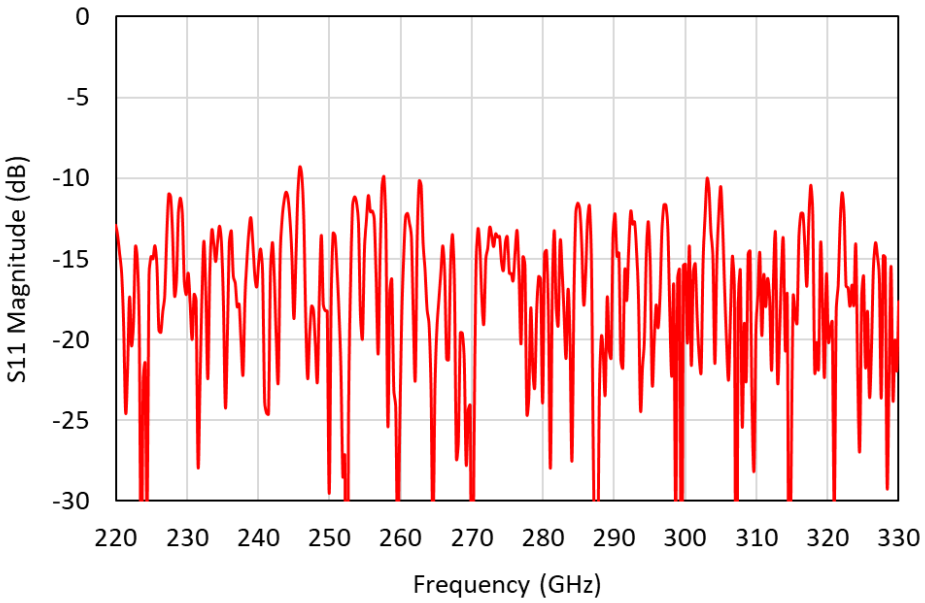

Figure 61. Measured Phase Delay Line antenna return loss.

The following table shows a summary of the results regarding the KPIs.

Table 7. KPIs requirements and measured results of PDLA.

KPI	Requirement	Measured Result – Phase Delay Line Antenna
Return loss	< -10 dB	< -10 dB
Directivity	> 14 dBi	> 20 dBi (according to gain diagram)
Steering angle	20 to 50 degrees	60 degrees
Losses	< 2 dB	17 dB

4 Conclusions

In conclusion, the document details the successful design, fabrication, and characterization of both high directivity and beam steering antennas intended for the TIMES project's Proofs of Concept. The validation results indicate that the high gain antenna meets the requirements for PoC 1, achieving a directivity exceeding 50.5 dBi and maintaining a return loss below -10 dB across the entire 220-330 GHz band. The measured beamwidth is also significantly less than the KPI requirement.

For PoC 2, two distinct beam steering antenna designs are explored: the Leaky Wave Antenna (LWA) and the Phase Delay Line Antenna (PDLA). The LWA demonstrates a steering performance of 0.34° per GHz and achieves a gain of over 10 dB in the frequency range of 260 GHz to 310 GHz. The return loss for the LWA is within acceptable limits across the operational bandwidth. Specifically, it remains below -8 dB in the higher frequency portion of its intended operational range.

The PDLA exhibits a higher steering capability of 2° per GHz with a gain exceeding 8 dB between 295 GHz and 300 GHz. The measured return loss for the PDLA is good, staying below -10 dB across the operational bandwidth. However, it is observed that the gains for both steering antennas are lower than initially simulated, a factor that will need to be carefully considered in the link budgets for PoC 2.

Despite the gain discrepancies in the beam steering antennas, the successful fabrication and validation of these prototypes provide valuable and functional components for the future Proofs of Concept of the TIMES project. Ongoing investigations are underway at Anteral to understand and mitigate the sources of gain reduction in the beam steering antennas. The results presented in this deliverable represent a significant step towards the practical implementation and evaluation of THz industrial mesh networks.

5 References

[1] Antenna Theory: Analysis and Design, (ISBN-10: 1118642066).

[2] “Deliverable D2.1. Definition of use cases, KPIs, and scenarios for channel measurements”.

[3] “Deliverable D2.3. Definition of scenarios and KPI for hardware demonstration and PoC”.

[4] G. I. Kweon and C. H. Kim, “Aspherical lens design by using a numerical analysis,” *J. Korean Phys. Soc.,* vol. 51, no. 1, pp. 93-103, 2007.

[5] “https://www.ticra.com/software/grasp/,” [Online].

[6] “https://www.3ds.com/products/simulia/cst-studio-suite,” [Online].

[7] Antenna Engineering Handbook, (ISBN-13: 978-0071475747).

[8] Terahertz Beam Steering: from Fundamentals to Applications, (DOI: 10.1007/s10762-022-00902-1).

[9] O. Goldstone and A. A. Oliner, “Leaky-Wave Antennas I: Rectangular Waveguides,” *IRE Trans. Antennas Propag.,* vol. 7, no. 4, 1959.

[10] C. H. Walter, Traveling Wave Antennas, McGraw Hill, 1965.